



**Calhoun: The NPS Institutional Archive**  
**DSpace Repository**

---

Theses and Dissertations

1. Thesis and Dissertation Collection, all items

---

1995-03

# Total dose radiation effects on hardened SOI bipolar transistors using the NPS Linac

Brittain, Donald R.

Monterey, California. Naval Postgraduate School

---

<http://hdl.handle.net/10945/31523>

---

This publication is a work of the U.S. Government as defined in Title 17, United States Code, Section 101. Copyright protection is not available for this work in the United States.

*Downloaded from NPS Archive: Calhoun*

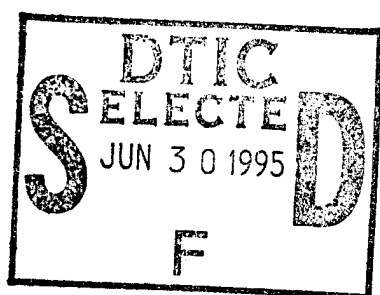


<http://www.nps.edu/library>

Calhoun is the Naval Postgraduate School's public access digital repository for research materials and institutional publications created by the NPS community. Calhoun is named for Professor of Mathematics Guy K. Calhoun, NPS's first appointed -- and published -- scholarly author.

**Dudley Knox Library / Naval Postgraduate School**  
**411 Dyer Road / 1 University Circle**  
**Monterey, California USA 93943**

# NAVAL POSTGRADUATE SCHOOL MONTEREY, CALIFORNIA



## THESIS

**TOTAL DOSE RADIATION EFFECTS  
ON HARDENED SOI BIPOLAR TRANSISTORS  
USING THE NPS LINAC**

by

Donald R. Brittain, Jr.

March, 1995

Thesis Advisor:

Sherif Michael

Approved for public release; distribution is unlimited.

DTIC QUALITY INSPECTED 5

19950629 039

REPORT DOCUMENTATION PAGE			Form Approved OMB No. 0704-0188	
Public reporting burden for this collection of information is estimated to average 1 hour per response, including the time for reviewing instruction, searching existing data sources, gathering and maintaining the data needed, and completing and reviewing the collection of information. Send comments regarding this burden estimate or any other aspect of this collection of information, including suggestions for reducing this burden, to Washington Headquarters Services, Directorate for Information Operations and Reports, 1215 Jefferson Davis Highway, Suite 1204, Arlington, VA 22202-4302, and to the Office of Management and Budget, Paperwork Reduction Project (0704-0188) Washington DC 20503.				
1. AGENCY USE ONLY (Leave blank)		2. REPORT DATE March 1995		3. REPORT TYPE AND DATES COVERED Master's Thesis
4. TITLE AND SUBTITLE TOTAL DOSE RADIATION EFFECTS ON HARDENED SOI BIPOLAR TRANSISTORS USING THE NPS LINAC			5. FUNDING NUMBERS	
6. AUTHOR(S) Brittain, Donald R. Jr.				
7. PERFORMING ORGANIZATION NAME(S) AND ADDRESS(ES) Naval Postgraduate School Monterey CA 93943-5000			8. PERFORMING ORGANIZATION REPORT NUMBER	
9. SPONSORING/MONITORING AGENCY NAME(S) AND ADDRESS(ES)			10. SPONSORING/MONITORING AGENCY REPORT NUMBER	
11. SUPPLEMENTARY NOTES The views expressed in this thesis are those of the author and do not reflect the official policy or position of the Department of Defense or the U.S. Government.				
12a. DISTRIBUTION/AVAILABILITY STATEMENT Approved for public release; distribution is unlimited.			12b. DISTRIBUTION CODE	
13. ABSTRACT (maximum 200 words) Silicon-on-insulator bipolar transistors fabricated using the Harris UHF-1 process, were irradiated at room temperature with 30 and 60 MeV electron beams. Some of the transistors on each die were configured and biased as a simple operational amplifier (opamp), one was placed in a common emitter type circuit and the remaining were biased to measure transistor parameter degradation. The purpose of this setup was to observe the total dose effects of the transistor and of an opamp on the same die in order to derive a more accurate model of an opamp under total dose conditions. This investigation was successful in conducting in-situ measurements of opamp gain and 3dB frequency while also measuring the current gain of similar transistors on the same die.				
14. SUBJECT TERMS Operational Amplifiers, Radiation Effects in Electronic Devices, Bipolar, Total Dose Radiation Effects, Naval Postgraduate School			15. NUMBER OF PAGES 94	
			16. PRICE CODE	
17. SECURITY CLASSIFICATION OF REPORT Unclassified	18. SECURITY CLASSIFICATION OF THIS PAGE Unclassified	19. SECURITY CLASSIFICATION OF ABSTRACT Unclassified	20. LIMITATION OF ABSTRACT UL	

NSN 7540-01-280-5500

Standard Form 298 (Rev. 2-89)  
Prescribed by ANSI Std. Z39-18 298-102



Approved for public release; distribution is unlimited.

TOTAL DOSE RADIATION EFFECTS ON HARDENED SOI BIPOLAR  
TRANSISTORS USING THE NPS LINAC

by

Donald R. Brittain, Jr.  
Lieutenant, United States Navy  
B.S., Virginia Tech, 1987

Submitted in partial fulfillment  
of the requirements for the degree of

**MASTER OF SCIENCE IN ELECTRICAL ENGINEERING**

from the

**NAVAL POSTGRADUATE SCHOOL**  
**March 1995**

Author:

\_\_\_\_\_  
Donald R. Brittain, Jr.

Approved by:

\_\_\_\_\_  
Sherif Michael, Thesis Advisor

\_\_\_\_\_  
Douglas J. Fouts, Second Reader

\_\_\_\_\_  
Michael A. Morgan, Chairman  
Department of Electrical and Computer Engineering



## ABSTRACT

Silicon-on-insulator bipolar transistors fabricated using the Harris UHF-1 process, were irradiated at room temperature with 30 and 60 MeV electron beams. Some of the transistors on each die were configured and biased as a simple operational amplifier (opamp), one was placed in a common emitter type circuit and the remaining were biased to measure transistor parameter degradation. The purpose of this setup was to observe the total dose effects of the transistor and of an opamp on the same die in order to derive a more accurate model of an opamp under total dose conditions. This investigation was successful in conducting in-situ measurements of opamp gain and 3dB frequency while also measuring the current gain of similar transistors on the same die.

Accession For	
NTIS CRA&I	<input checked="checked" type="checkbox"/>
DTIC TAB	<input type="checkbox"/>
Unannounced	<input type="checkbox"/>
Justification .....	
By .....	
Distribution /	
Availability Codes	
Dist	Avail and/or Special
A-1	





## TABLE OF CONTENTS

I.	INTRODUCTION . . . . .	1
II.	RADIATION ENVIRONMENT AND ITS EFFECTS . . . . .	7
	A. FORMS OF RADIATION AND THEIR INTERACTION . . .	7
	B. RADIATION IN SPACE . . . . .	12
	1. Historical Background . . . . .	12
	2. Types of Space Radiation and Its Sources . . .	15
	a. Cosmic Rays . . . . .	15
	b. Solar Plasma . . . . .	17
	c. Van Allen Belts . . . . .	18
	3. The Magnetosphere and the Van Allen Belts . . . . .	19
	4. Outside the Van Allen Belts . . . . .	22
III.	TRANSIENT EFFECTS OF RADIATION ON ELECTRONIC SYSTEMS (TREE) . . . . .	25
	A. INTRODUCTION . . . . .	25
	B. OVERVIEW OF SEMICONDUCTOR PHYSICS . . . . .	25
	C. FORMATION AND CHARACTERISTICS OF A PN JUNCTION . . . . .	35
	D. RADIATION EFFECTS IN A BIPOLAR TRANSISTOR . . .	38
IV.	EXPERIMENTAL APPROACH . . . . .	41
	A. OVERVIEW OF THE NPS LINAC . . . . .	41
	B. DOSIMETRY . . . . .	42
	1. Overview . . . . .	42
	2. Application of TLD Dosimetry . . . . .	44
	C. DESCRIPTION OF THE DEVICE UNDER TEST . . . . .	47
	D. CIRCUIT DESIGN . . . . .	48
	1. Design of the Operational Amplifier . . .	49
	2. Common Emitter Circuit . . . . .	50

3. Measurement of DC Current Gain ( $\beta$ ) . .	52
E. EXPERIMENTAL SETUP . . . . .	53
V. RESULTS . . . . .	61
VI. CONCLUSIONS AND RECOMMENDATIONS . . . . .	75
APPENDIX. GLOSSARY OF SYMBOLS AND TERMS . . . . .	77
LIST OF REFERENCES . . . . .	81
INITIAL DISTRIBUTION LIST . . . . .	85

## I. INTRODUCTION

The subject of radiation effects on electronic material has been a heavily studied subject since the early 1960's and especially since the Starfish nuclear event (1962) which increased the radiation levels in the Van Allen belts, resulting in the failure of several satellites in orbit [Ref. 1, p. 1527]. The degradation of bipolar transistor current gain caused by ionizing radiation was the cause of these satellite failures [Ref. 2, p.1540]. Interest in this subject is still high and rightly so, since almost every aspect of our lives depends on electronic devices, more of which are being deployed on spacecraft.

Now there is even a greater variety of electronic components and circuits with an ever increasing complexity and range of failure mechanisms. These circuits and devices are being used extensively in space, where there is often a harsh radiation environment, even in the absence of a nuclear detonation. In order to ensure that spacecraft can complete their mission safely and effectively, there must be a thorough understanding of the mechanisms that cause failure in electronic components.

Regardless what is sent into space, it will be exposed to a certain amount of radiation over its useful life. A designer of space products needs to know how materials, specifically semiconductors and shielding materials, will react given a certain dose of radiation. In order to fabricate an effective device to withstand radiation, radiation models need to be developed for the particular kinds of devices utilized.

In order to design a device or circuit for in space or other radiation environment there must be an awareness of the types and levels of radiation in the operating environment. The nature of the space radiation environment (the environment

of concern in this paper) cannot be understood with a simple model. For example: the total dose received in ten hours inside Spacelab on a low altitude Space Shuttle flight was  $10^{-1}$  rad while it was expected to receive up to  $10^8$  rads in one hour at the closest approach to Jupiter on the Galileo flight [Ref. 1, p.1530]. Orbits in the somewhat homogeneous trapped radiation belts can experience sudden changes in dose due to solar flares occurring during various times of the year. Figure (1.1) shows the dose/year for aluminum as a function of altitude for a particular orbit. As can be seen, the nature of space radiation will lead to the discovery that it is a function of both space and time.

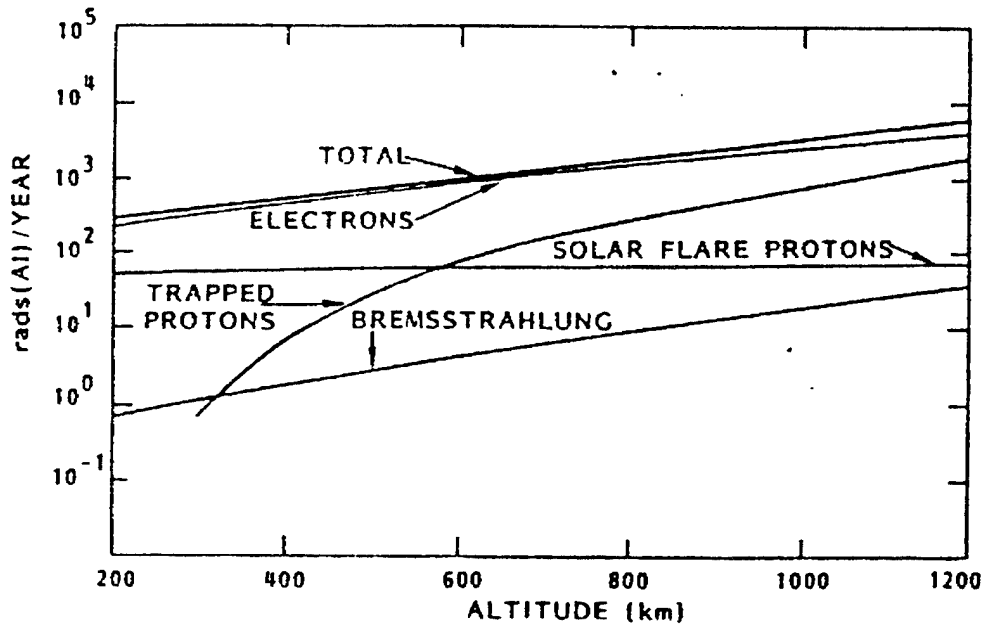


Figure 1.1. Dose rate versus altitude for a circular orbit at 600 inclination. From Ref. [2, p. 1511].

The space radiation environment for orbits up to the geosynchronous orbits can be broken down into three sources: trapped radiation belts (Van Allen belts) consisting of protons and electrons, solar flares and cosmic rays (mostly from outer galactic sources). These sources can result in

dielectric ionization (total dose effects), transient ionization and displacement damage. The nature of the space radiation environment is further discussed in Chapter II.

Of the three above effects, displacement damage is most predictable. This affects primarily solar cells and wide-base bipolar transistors (used mostly in power applications). Transient ionization (single particle effects) causes what is known as single event upset (SEU) in MOS type memory devices.

Dielectric ionization or total dose effects were the first to cause failure in the space radiation environment and continue to cause problems in more advanced and high density microelectronic circuits. In this research, where bipolar devices are of concern, the major effect of ionization is an increase in surface recombination velocity which ultimately degrades current gain. Chapter III discusses this effect in further detail.

From the above discussion, it can be seen that radiation testing is a necessity for the design of space applications. The goals of radiation testing are best summarized by Pease:

The objectives of radiation testing are threefold: 1) understand the mechanisms of the interaction of the radiation with electronic materials and how these effects relate to device failure; 2) characterize the response of specific device types and technologies for use in part selection for specific systems application; and 3) determine the acceptability of production lots for use in deployable systems. [Ref.2, p. 1514]

The goal of this research is reflected by the first objective above. More specifically, we want to form an accurate model for a given technology that can predict the response of operational amplifiers to total dose radiation. The approach taken is to first investigate the response of individual components of the opamp (transistors in this research) and apply these results to form a model for an opamp by way of

superposition of the responses of individual components. It is imperative then, to validate this data by exposing the opamp to the same radiation environment as the individual components. To accurately do this, the opamp and separate components must be on the same die and certain device parameters and circuit design of the opamp must be known (this can sometimes be difficult due to manufacturer proprietary reasons). This research is primarily directed to a proof-of-concept of the above.

The obvious method for radiation testing would be to put the device or circuit in the actual environment and monitor it. This is done in fact (Combined Release and Radiation Effects Satellite (CRRES)), however the time required and costs can be excessive and the type of data that can be acquired is limited [Ref. 2, p.1514]. Therefore, alternative solutions must be sought.

Reproduction of the space environment in the laboratory can be difficult and expensive. More commonly, a single radiation source is used to isolate the dominant effect in a particular space environment. The damage in a total dose environment is mainly caused by ionization energy absorbed by the material. This type of damage can be simulated with electrons or photons. More costly proton sources can also be used, but the disadvantage is that displacement effects must be differentiated from the ionization effects. Table 1.1 summarizes different total dose simulator characteristics and their comparison with the space environment.

Since this research is concentrating on total dose effects, the simulation used in this experiment was conducted using 30 and 60 MeV electrons generated by the NPS Linear Accelerator (LINAC). In addition, in-situ (sometimes referred to as in-flux) testing was utilized. This method involves taking the device parameter measurements while it is being irradiated under normal operating conditions. Another method,

	Particle Type	Energy	Range of Dose Rates rad (SiO <sub>2</sub> )/s	Pulse Width
Dynamitron	electrons	2.5 MeV	10 <sup>2</sup> -10 <sup>7</sup>	1 ms-dc
LINAC	electrons	5-60 MeV	$\begin{cases} 10^5-10^{10} \\ 10^6-10^{11} \end{cases}$	1-10 $\mu$ s 10-100 ns
<sup>137</sup> Cs	photons	670 keV	10 <sup>-2</sup> -10 <sup>2</sup>	dc
<sup>60</sup> Co	photons	1.1 MeV	10 <sup>-2</sup> -5 $\times$ 10 <sup>2</sup>	dc
X-ray tubes	photons	10 keV to > 100 keV	10 <sup>1</sup> -10 <sup>4</sup>	dc
Space	electrons, photons, protons	< 1 MeV to > 100 MeV	< 10 <sup>-1</sup> ave.	variable

Table 1.1. Total dose simulator characteristics compared to the space ionization environment. From Ref. [2, p. 1516]

step-stress testing, involves taking measurements, irradiating the device and then retaking the measurements for comparison. This method is a lot simpler than the in-situ method but the results are considered to be less precise [Ref. 2, p. 1515].

The testing in this research consisted of irradiating silicon-on-insulator (SOI) bipolar transistors biased for current gain measurements, implemented in a simple operational amplifier configuration and in a common emitter configuration. All transistors were co-located on a single die to ensure the same radiation exposure. The complete description of this experiment is contained in Chapter IV. In Chapter V the results are discussed and the conclusions and recommendations for further research are found in Chapter VI.





## II. RADIATION ENVIRONMENT AND ITS EFFECTS

### A. FORMS OF RADIATION AND THEIR INTERACTION

In the space radiation environment there are many forms of radiation that may affect vital electronic components in spacecraft (specifically satellites). Electrons, protons, gamma rays, alpha and beta particles and heavy ions are of primary concern. These forms of radiation can be categorized into two types: photons (electromagnetic waves) and particles.

Electromagnetic waves consist of discrete quanta of energy  $h\nu$ , where  $h$  is Planck's constant and  $\nu$  is the frequency. These quanta are called photons and are used to describe the particle-like nature of electromagnetic radiation. A photon can be considered a particle with zero rest mass and neutral charge. Two examples of photons are gamma rays and X-rays. There are three types of interactions a photon can have on matter: the photoelectric effect, Compton scattering and pair production.

The photoelectric effect was first observed by Heinrich Hertz in 1887 and further investigated by Lenard in 1900. When light of frequency  $\nu$  is incident on a clean metal surface, electrons are emitted with a maximum energy described by the Einstein equation:

$$E = eV_0 = \frac{1}{2}mv^2 = h\nu - \phi_0 \quad (2.1)$$

where  $V_0$  is the stopping potential,  $m$  is the mass of an electron,  $v$  is the velocity of the electron and  $\phi_0$  is the energy required to remove an electron from the surface of the metal (work function). Figure (2.1) shows the experimental setup for the photoelectric effect and a plot of the observed photocurrent vs. stopping potential  $V_0$ . [Ref. 3, pp. 107-109]

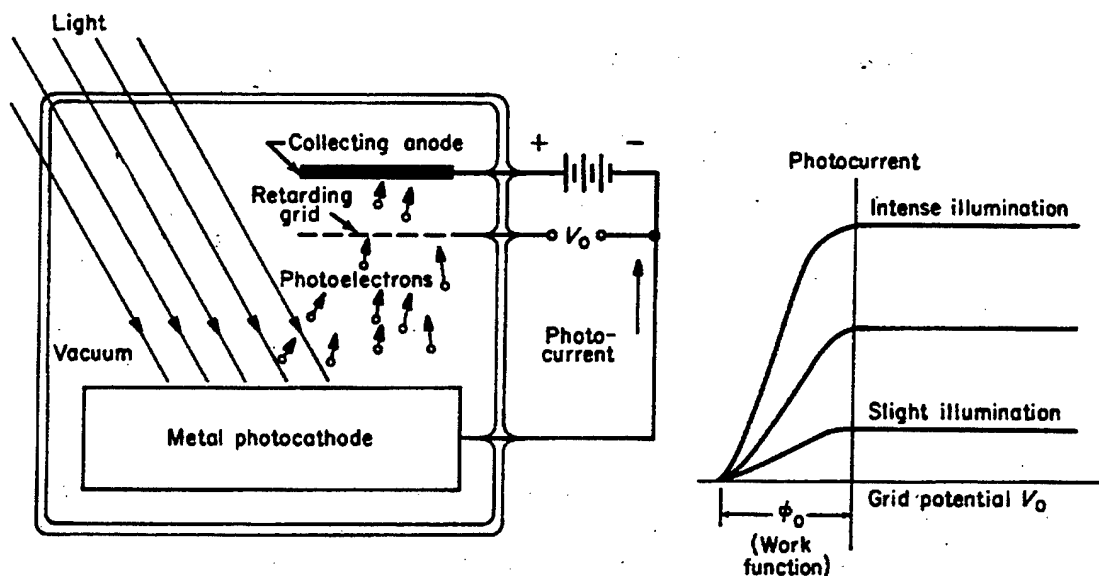


Figure 2.1. Photoelectric effect. From Ref. [4, p. 66].

From Equation (2.1), it can be seen that for the photoelectric effect to occur, the incident photon must have energy at least greater than some threshold energy  $h\nu_0$ , regardless of the incident photon intensity. In this case, the number of emitted electrons (sometimes called photoelectrons) are proportional to the incident light intensity and have frequency  $\nu - \nu_0$ . Otherwise the incident light energy will just increase the kinetic energy of the electrons, resulting in a temperature increase without the release of electrons. Note that Equation (2.1) only gives the maximum energy given the incident monochromatic frequency. The actual energy of the electrons leaving the surface may be less due to energy loss transversing the finite thickness of the metal. [Ref. 3, pp. 107-108] [Ref. 4, p. 66]

Compton scattering is another phenomenon demonstrating the particle nature of electromagnetic radiation. When a photon of energy  $h\nu$  and momentum  $p = h\nu$  ( $\lambda = c/\nu$ ) collides with an electron, the photon is scattered by an angle of  $\theta$  and loses part of its energy to the recoiling electron. This

transfer of energy is reflected by a decrease in the frequency of the photon and is related by the following equation:

$$\lambda_2 - \lambda_1 = \frac{h}{mc} (1 - \cos\theta) \quad (2.2)$$

where  $\lambda_1$  and  $\lambda_2$  are the photon wavelengths before and after the collision respectively. Figure (2.2) illustrates this effect.  $E_0 = mc^2$  is the energy of the electron at rest and  $E = (E_0^2 + p_e^2 c^2)^{1/2}$  is the energy of the electron after the collision. [Ref. 4, pp.115-116]

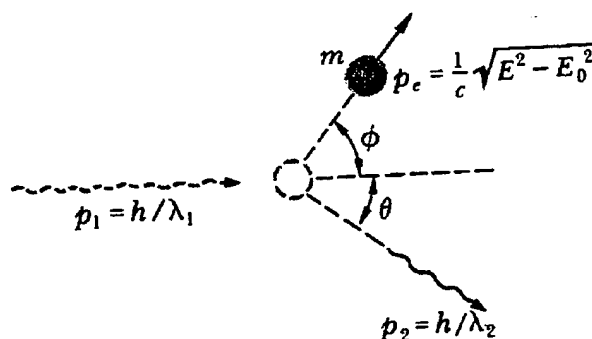


Figure 2.2. Compton scattering. From Ref. [3, p. 116].

When a photon of sufficiently high energy passes nearby an atomic nucleus, the nucleus recoils and an electron-positron (has properties of an electron but possesses a positive charge) pair is formed. This process is called pair production or materialization. The positron is only transitory and will soon interact with an electron forming two or three gamma rays (the formation of one gamma ray would prohibit the simultaneous conservation of energy and momentum) [Ref. 5, p. 922]. The incident photon is annihilated in the process. If the recoil of the nucleus is absorbed by an electron, a triplet is formed consisting of two electrons and

a positron. Figure (2.3) is a photograph of hydrogen bubble chamber used for observing elementary particles. In upper half of Figure (2.3), three tracks can be seen to originate from a common point. This is where the photon interacts with the nucleus and is annihilated producing a triplet consisting of an electron-positron pair (the circular paths) and another electron. In the lower half of the figure, two tracks can be seen, originating from another common point (the circular paths are not visible). This is the electron-positron pair without the extra electron. Observe that the triplet electron-positron pair tracks curve in opposite directions. Since the bubble chamber is in a magnetic field, comparison of the two tracks indicate that the two particles have opposite charges. Both particles are shown to ionize like electrons in the chamber, thus proving the existence of a positron. The threshold energy for this process is 1.022 MeV. [Ref. 5, p. 589] [Ref. 6, p. 55] [Ref. 7, p.479]

The energy of the photon determines which of the above interactions dominate. In the case of silicon, the photoelectric effect dominates at photon energies less than 50 keV. Between 50keV and 20MeV Compton scattering dominates. When photon energies are greater than 20MeV, pair production dominates. [Ref. 8, p. 1444]

Charged particles interact with matter quite differently than photons. Elastic collisions occur between charged particles and atoms called Rutherford scattering. In particular, the nucleus of one atom will scatter particles at a certain angle  $\theta$  that are incident at a distance  $b$  from the axis of the atom (see Figure 2.2). This occurs only if the particles do not have enough energy to penetrate the nucleus of the atom.

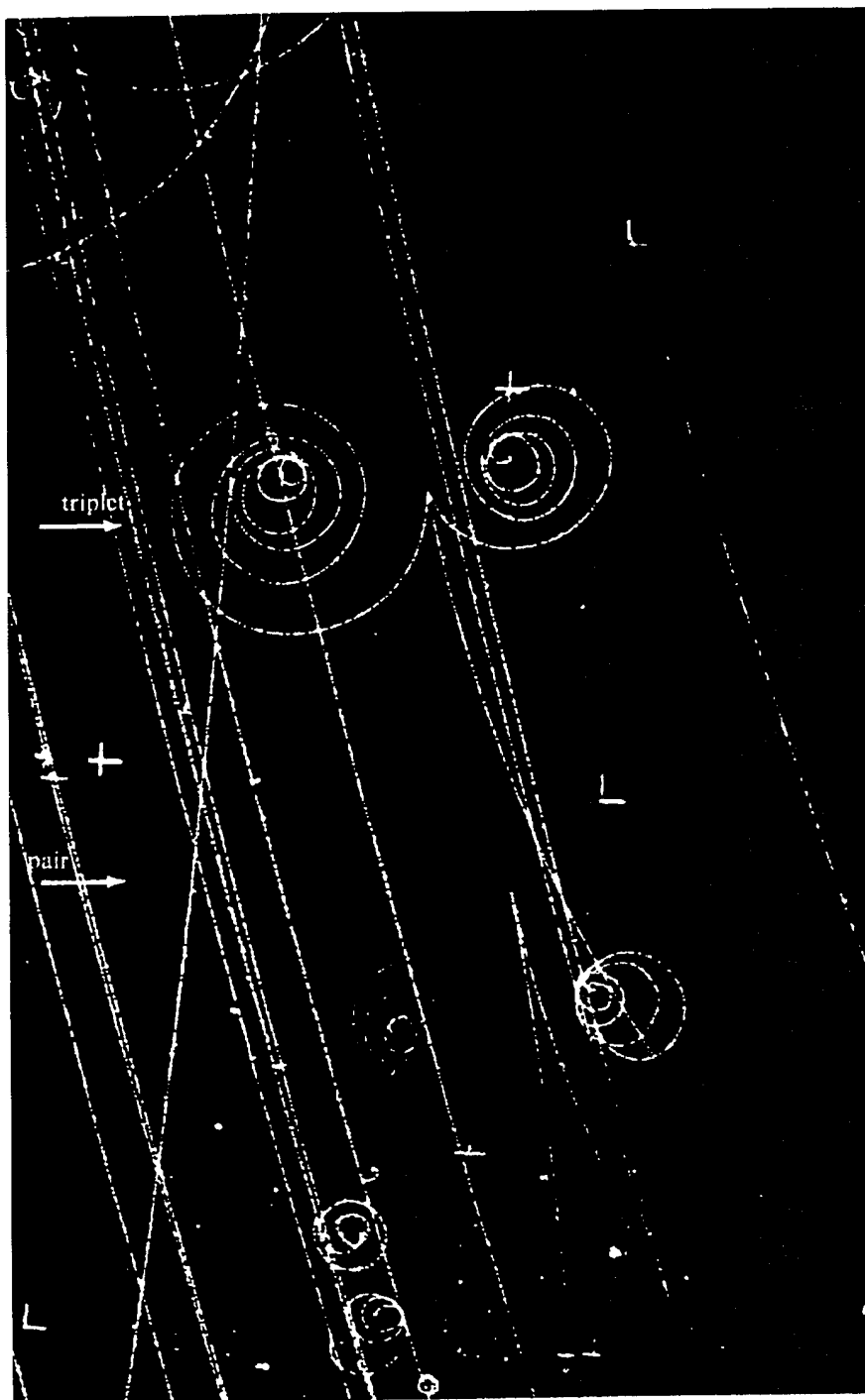


Figure 2.3. Pair production in a hydrogen bubble chamber. Tracks show formation of triplet and pair. From Ref [6, p. 56].

The following Rutherford scattering equation describes this interaction [Ref:2, p.23]:

$$b db = \left( \frac{Ze^2}{4\pi\epsilon_0 mv^2} \right)^2 \frac{\sin\theta d\theta}{\sin^4\left(\frac{\theta}{2}\right)} \quad (2.3)$$

Note that Equation (2.3) is derived assuming that the nucleus is a point charge. This is not the physical case but the equation holds true so long as the incoming particle does not penetrate the nucleus. [Ref. 3, p.138-139]

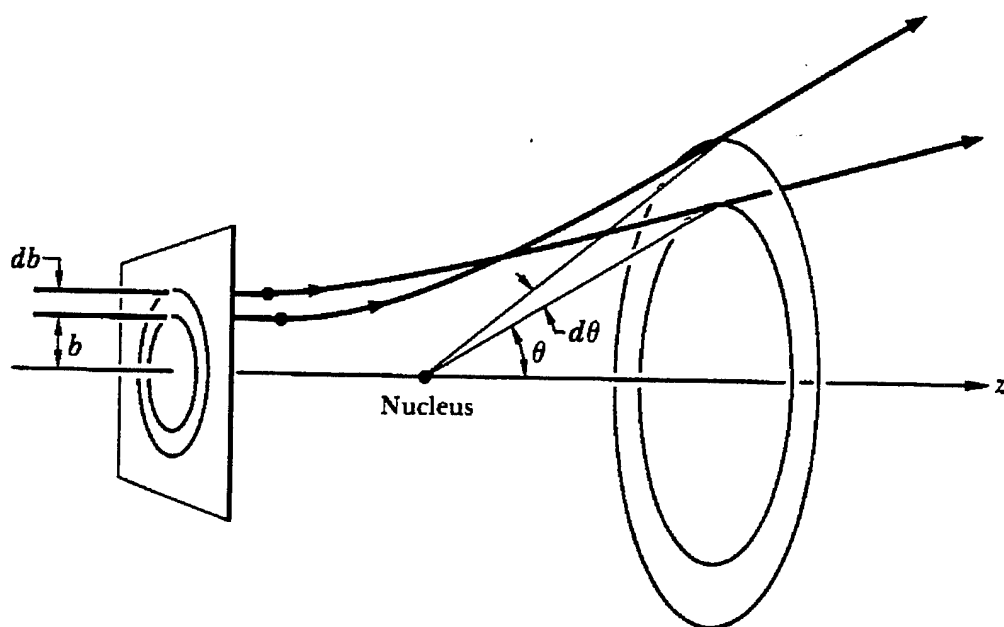


Figure 2.4. Rutherford scattering. From Ref. [1, p. 139].

## B. RADIATION IN SPACE

### 1. Historical Background

In the 1950's, the scientific community's perception of the earth's magnetic field was that it was like a bar magnet as in Figure (2.5) and that it became weaker as it extended thousands of miles into space.

In addition, cosmic rays were known to reach the earth at the time but were thought to originate from somewhere in space other than the sun (which was believed only to emit visible light) since the rays were isotropic. It wasn't until the use of rockets and orbiting satellites that the nature of space radiation was revealed. [Ref. 9, p.2]

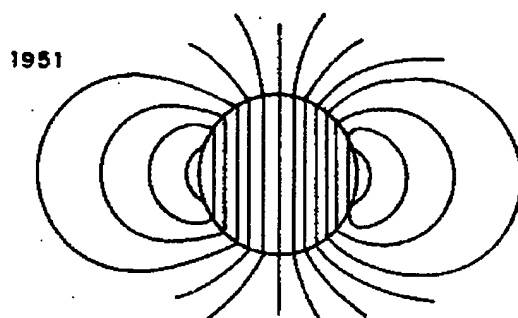


Figure 2.5. Early view of the Earth's magnetic field Ref [13, p. 4-2].

After much political turmoil with the U.S. satellite program Project Vanguard, Explorer I was finally launched on January 31, 1958 carrying a Geiger counter provided by Professor Van Allen's group in Iowa. There was no recorder on board Explorer I, so data had to be recorded by receiving stations during satellite overpasses which were approximately 2 minutes in length. The data received from Explorer I revealed that over South America at high altitudes of over 2000 km, there appeared to be no cosmic rays. However, at low altitudes of 500 km, the normal cosmic ray count of 30 counts/sec was observed. The Iowa group could not come up with an explanation for this. It wasn't until Explorer III was launched on March 26, 1958 that they found an answer. Since this satellite had a recorder on board, continuous data could be taken. At the beginning of the pass over South America, the count rate rapidly increased from the normal

cosmic ray level to recorder's limit of 128 counts/sec and then dropped to almost zero after seven minutes. About 10 minutes later, it increased sharply to 128 counts/sec. Carl McIlwain of the Iowa group explained that the counter had reached an area of a very high particle density and that the "dead-time effects of the counter reduced the count rate essentially to zero" [Ref. 9, pp. 5-9]. This explained the apparent absence of cosmic rays. In addition, Van Allen theorized that the increase in radiation over the cosmic level was due to trapped charged particles. This marked the beginning of the formulation of the Van Allen radiation belt model. Figure (2.6) shows Van Allen's first map of the radiation belt derived from two later satellites, Explorer IV and Pioneer III, which was published in 1959 [Ref 10, p. 39].

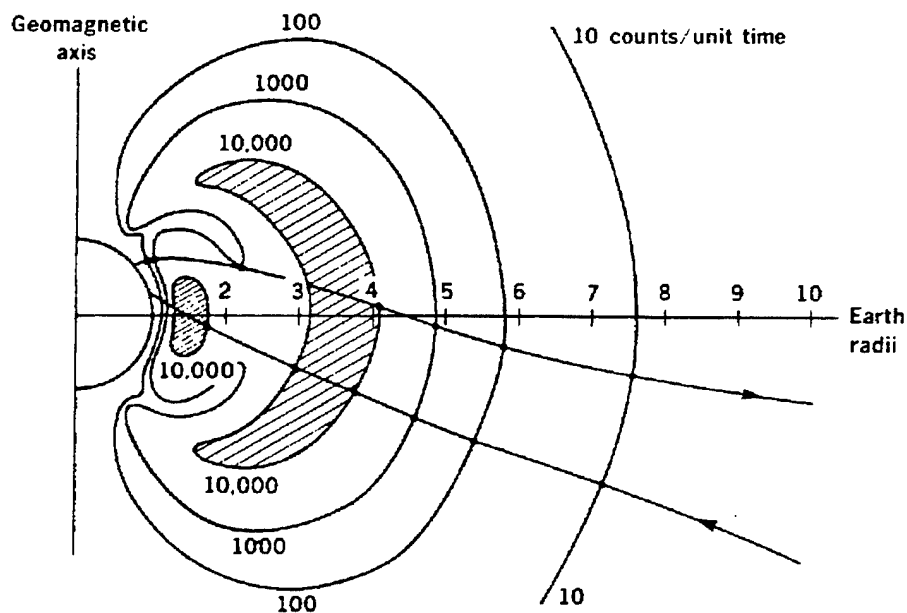


Figure 2.6. Van Allen's original map of the radiation belt. Constructed with data from Explorer IV and Pioneer III. From Ref [8, p. 39].



## 2. Types of Space Radiation and Its Sources

Radiation encountered in space can be broken down into three types or "sources": cosmic rays, geomagnetically trapped radiation near the earth (Van Allen belts) and solar plasma [Ref. 10, p.1]. Spacecraft will encounter some or all of these types of radiation depending on its orbit. Understanding of the spatial distribution and effects of each type of radiation is essential when designing systems to be utilized by the spacecraft.

### a. Cosmic Rays

Cosmic rays were first observed by Austrian physicist Victor Hess in 1911, using manned balloons at a maximum altitude of 17,500 feet. Since then many others including Robert Millikan conducted similar measurements at even higher altitudes, confirming "an extra terrestrial source of penetrating radiation." [Ref. 11, p.7]

A small amount of cosmic rays originate from the sun, where there are minor changes in flux from day to night, but the majority are from the Milky Way galaxy and even beyond where the sources are not exactly identified. Cosmic rays consist mostly (about 90%) of high-speed protons (the nuclei of the hydrogen atom), helium nuclei or alpha particles (9%), electrons (less than 2%) and gamma rays. [Ref. 7, p. 461]

Cosmic ray protons incident on the earth's atmosphere collide with nitrogen and oxygen nuclei forming secondary particles called  $\pi$ -mesons (mesons) which then decay rapidly (about  $10^{-8}$ sec) to  $\mu$ -mesons (muons). The  $\mu$ -mesons decay in about  $2 \times 10^{-6}$ sec to electrons (energies up to 50 MeV) and uncharged  $\mu$ -mesons decay into two gamma rays within  $10^{-8}$  sec. Hence, inbound cosmic rays to the earth's atmosphere form an avalanche or showers of electrons, gamma rays and various short-lived elementary particles. Figure (2.7) illustrates this effect. [Ref. 9, p. 70] [Ref. 11 pp. 12-13]

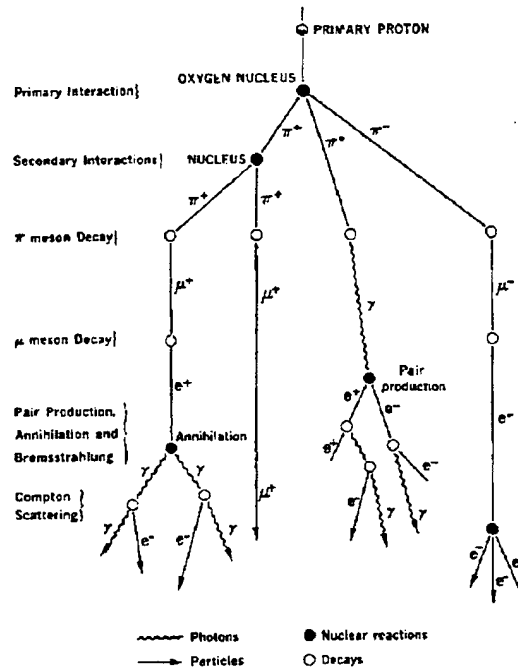


Figure 2.7. Cosmic Ray Avalanche. From Ref. [10, p. 5].

Neutrons are also produced by these cosmic ray proton collisions with the atmospheric nitrogen and oxygen nucleus. The neutron is radioactive with a mean life of about 1000 sec and decays as follows:

$$n \rightarrow p + \beta^- + \bar{\nu}_e \quad (2.4)$$

The antineutrino  $\bar{\nu}_e$ , was first introduced by Pauli in 1930 to explain the absence of conservation of energy in  $\beta$  decay and was observed in the laboratory in 1957. As far as space radiation is concerned, the important part of this decay is the resulting proton and  $\beta$  decay which is essentially the emission of a radioactive electron with a half life of about 10.8 min. The energy spectrum of the emitted electron is independent of the neutron's kinetic energy (assuming neutron energies less than 10MeV) and will have a  $\beta$  decay spectrum as shown in Figure (2.8). The resulting proton, on the other

hand will have kinetic energy almost identical to the parent neutron. This is because the electron's kinetic energy is almost the same as the mass difference between the neutron and electron. [Ref. 9, pp. 71-74]

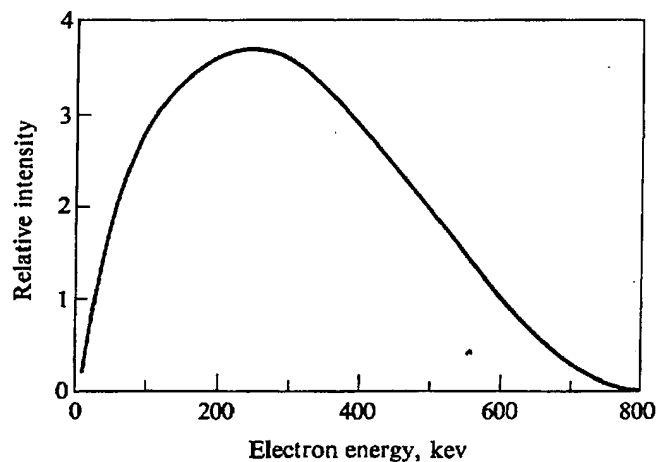


Figure 2.8. Beta decay spectrum.  
From Ref. [9, p.74].

Neutrons are also produced by the sun predominately by knock-on reactions in hydrogen and helium. However, it should be noted from the above discussion that very few neutrons actually make it to the earth's surface due to the short lifetime of the neutron. Figure (2.9) shows the measured neutron flux at various altitudes for various energies. [Ref. 9, pp. 72-73]

#### **b. Solar Plasma**

Plasmas are regions of particles, charged and uncharged, that when exposed to a static electric fields redistribute themselves so that they are shielded from the field. On the boundary of plasmas are strong field regions called sheaths. An important property of plasmas is that they tend to remain electrically neutral. [Ref. 12, p.291]

Solar plasma, as the name implies, originates from the sun and consists of equal numbers of electrons and

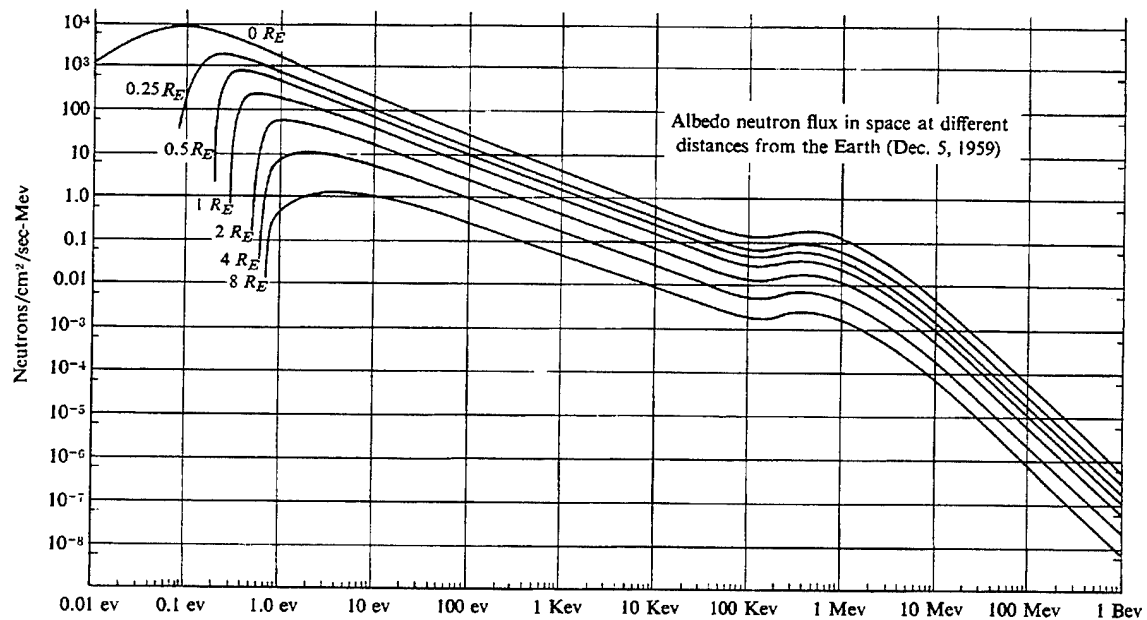


Figure 2.9. Neutron-energy spectrum at different distances above the geomagnetic equator. The top of the atmosphere is labeled  $0 R_E$  (approx. 100km). From Ref. [7].

positive ions. It is actually a continuation of coronal expansion and begins at a very slow speed at the corona but becomes supersonic at 10-20 solar radii ( $6.96 \times 10^5$  km). This is what comprises solar wind whose effects will be described in the next section.

### c. Van Allen Belts

Strictly speaking the radiation belts are not actually a source of radiation. The effect and interaction that the magnetosphere and atmosphere has on incident radiation can give the appearance that the radiation belts are a source. Understanding these radiation belts is critical because of the number of satellites in this region. Low earth orbits (LEO's) include altitudes of 90 to 500 miles. Satellites in LEO's include weather satellites, space shuttle, space telescope, earth resources satellites and space stations. In addition, Global Positioning Satellites (GPS) orbit at about 12,000 miles, which is within the outer Van

Allen belt. Because of its complexity and importance, Van Allen belts are treated separately in the next section.

### 3. The Magnetosphere and the Van Allen Belts

The natural trapped radiation environment in orbits about the earth (altitudes to about 32,000 km) as we know it today consist of electrons protons and a lesser number of heavy, low energy ions. The earth's magnetic lines of force are constrained to a region of influence or cavity called the magnetosphere by the continuous flow of charged particles (the solar plasma) from the sun called solar wind. The outer boundary of this region is known as the magnetopause (Refer to Figure (2.10)). The pressure of solar wind shapes this magnetosphere. As a result, the daylit side is compressed and the night side is expanded as shown in Figure (2.10).

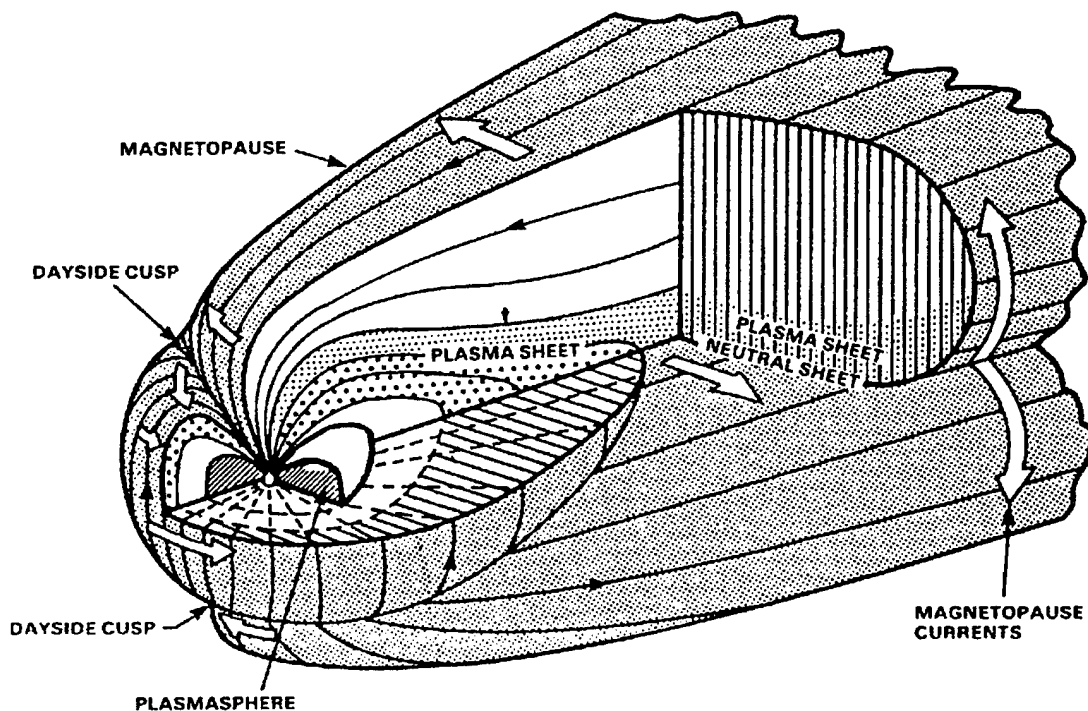


Figure 2.10. Magnetosphere. From Ref. [14, p. 1424 ].

The magnetosphere can be divided into five regions according to the particles predominating as shown in Figure (2.11). The boundaries of these regions are not to be interpreted as sharp interfaces but diffused areas changing in position due to various solar and other variations.

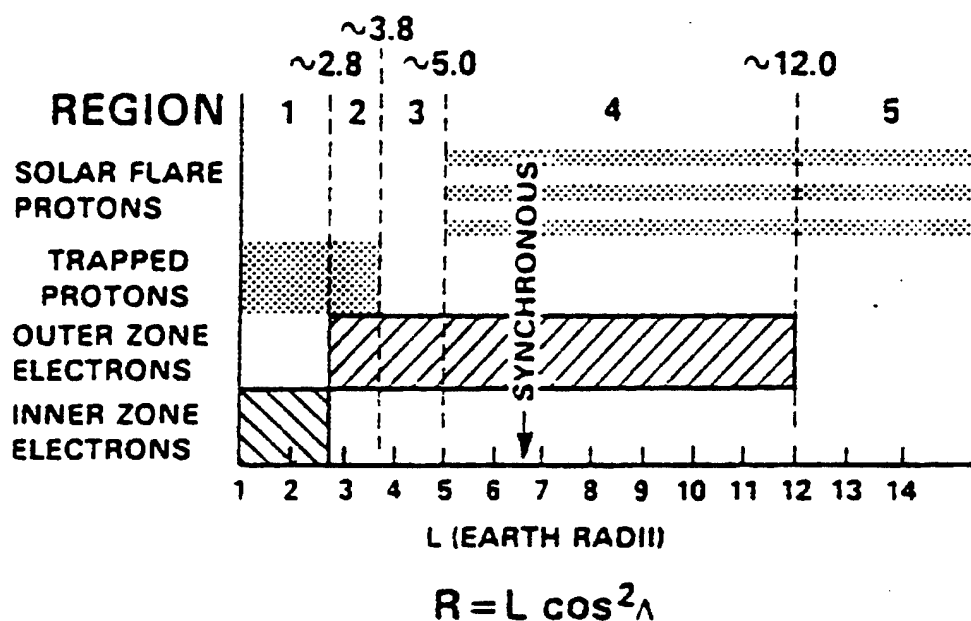


Figure 2.11. Distribution of charged particles in the magnetosphere. From Ref. [8, p. 1425].

The path of charged particles from the sun or other sources approaching the magnetosphere will be altered by the field and tend to follow the field's lines of force. Particles below a critical energy become trapped and tend to spiral around these lines and bounce back and forth between reflection or mirror points (regions of maximum magnetic field

strength for a given path). Figure (2.12) illustrates this motion of particles. The charged particles (electrons and protons) that have become trapped within the plasmasphere region form what are called the Van Allen belts.

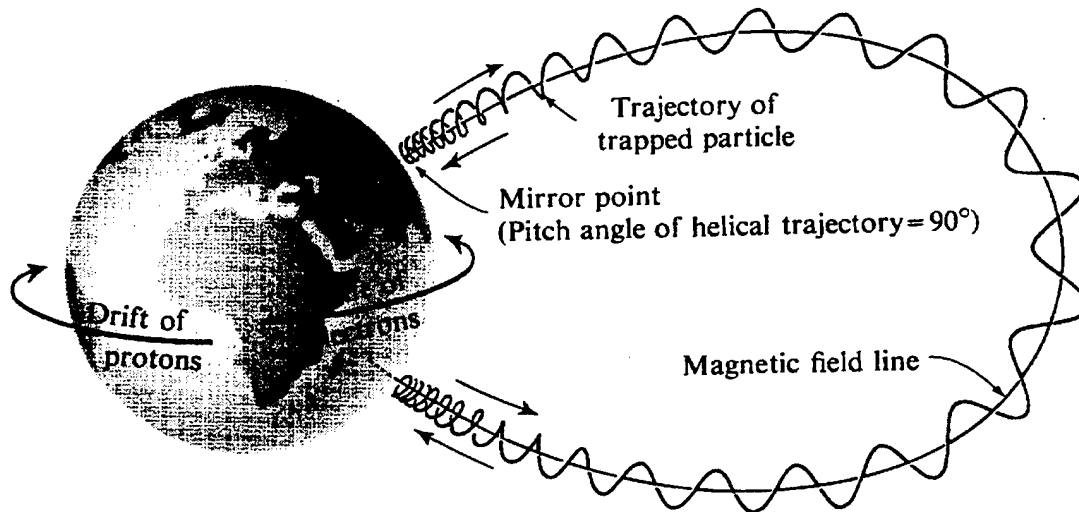


Figure 2.12. The motion of particles inside the trapped radiation belts. From Ref. [8, p. 1425].

A useful coordinate system, introduced by McIlwain in 1961, relates the magnetic field  $B$  to an adiabatic invariant (constant only for very slow changes of the variables involved) called the integral invariant  $I$ . The integral invariant is obtained from the longitudinal invariant  $J$  [Ref. 9, p.49]. The quantity  $I$  is the length of the field line between the reflection points described above. This coordinates system was designed to relate measurements made at physically different locations. McIlwain introduced the  $L$  parameter which is a dimensionless ration of the earth's surface, approximately the geocentric distance of a field line in the geomagnetic equator. The  $L$  parameter is given by:

$$L = R(\cos\lambda)^{-2} \quad (2.5)$$

where  $\lambda$  is the magnetic latitude [Ref. 13, p. 5-8].

The transformation of  $B$  is now given by:

$$B = \frac{M}{R^3} \sqrt{4 - \frac{3R}{L}} \quad (2.6)$$

where  $M$  is the geomagnetic dipole moment [Ref. 13, p. 5-8].

There is a particle flux dependence on latitude and altitude. In the lower latitudes, incoming particles are deflected sharply to follow the magnetic lines of force. Hence, only very high energy charged particles reach the low altitudes at low latitudes. At high latitudes, particles are already travelling along the lines of force (or nearly so) and therefore little deflection takes place. Even low energy particles achieve low altitudes at high latitudes. This is the reason for the depression of the Van Allen belts toward the earth's magnetic poles. Generally, the least radiative environment is at low inclinations (below  $28^\circ$ ) and low altitudes. This would correspond with the Low Earth Orbits (LEO). Figure (2.13) summarizes the radiation doses at  $28^\circ$ . [Ref. 14, p.1424]

#### **4. Outside the Van Allen Belts**

Geosynchronous equatorial orbits (GEO) at an altitude of 22,300 nautical miles, are essentially the highest orbits used by satellites. Many critical satellites such as military and commercial communication satellites, Defense Support Program (DSP) and Tracking and Data Relay Satellite System (TDRSS), utilize these orbits. Thus, it is essential to understand the radiation environment in this region of space. [Ref. 16, p. 141]

The outer limit of the trapped radiation would have to be where particles would no longer bounce between mirror points as was shown in Figure (2.9). This distance is about 10-12 earth radii on quiet days and does not change much with changes in the solar wind. However there are some regions in



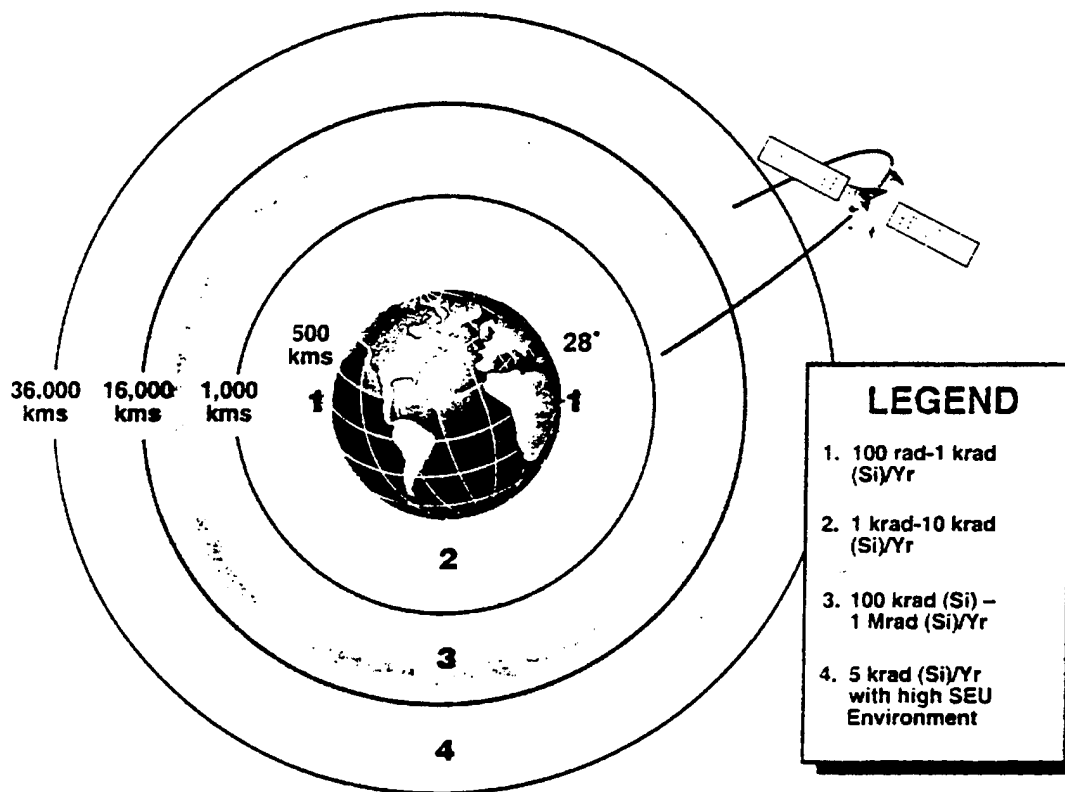


Figure 2.13. Summary of Radiation Doses. From Ref. [15, p. 2.2-4].

which particles whose path starts in the day side and overlaps in the night region where the field is no longer closed. These particles will be lost in the geomagnetic tail. This is called pseudotrapping and the regions where this occurs in shown in Figure (2.14). [Ref. 11, pp. 322-326]

The plasma sheet is made up of hot plasma that contains equal parts of hydrogen and oxygen ions. The electrons in this sheet have energies on the order of 10keV and can reach as high as 50-100keV during magnetic substorms. The plasma sheet is the normal environment for geosynchronous orbits. [Ref. 13, p. 5-17]

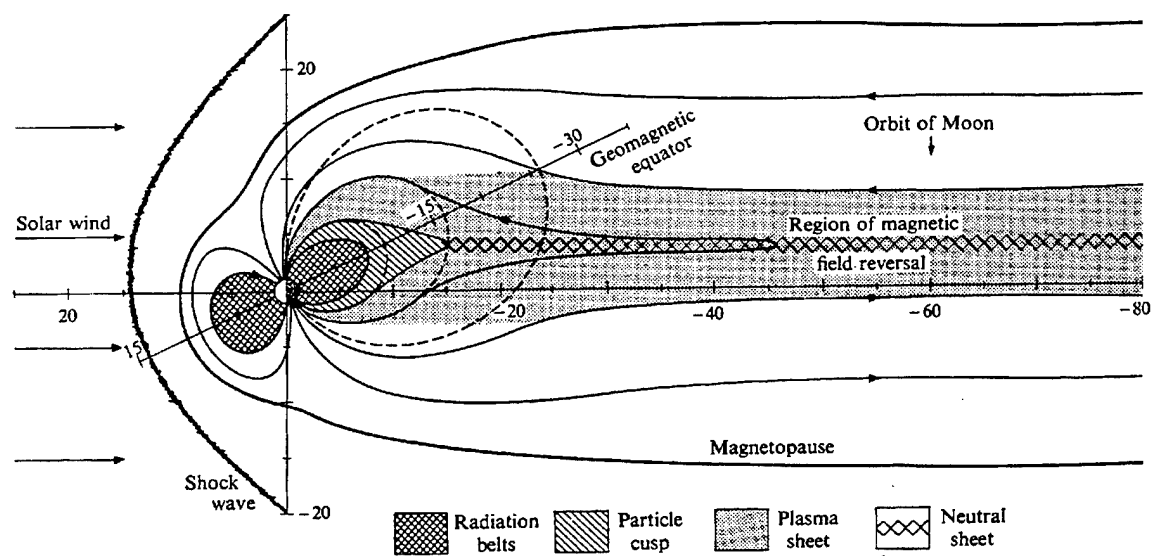


Figure 2.14. Geomagnetic-tail in the noon-midnight plane. From Ref [9, p. 334].

### III. TRANSIENT EFFECTS OF RADIATION ON ELECTRONIC SYSTEMS (TREE)

#### A. INTRODUCTION

Transient Effects of Radiation on Electronic Systems (TREE) is a general term associated with the effects of total dose, dose rate and neutron displacement in electronic devices. This chapter will attempt to provide a very brief introduction to the concepts of semiconductor physics and apply them to the basic operation of a bipolar transistor. Then the Transient Effects of Radiation on Electronic Systems (TREE) will be discussed for the specific case of the bipolar transistor.

#### B. OVERVIEW OF SEMICONDUCTOR PHYSICS

Silicon, a group IV element in the periodic table has four valence electrons which form covalent bonds with neighboring atoms resulting in a diamond crystalline structure called interlocking-face centered cubic [Ref. 17, pp. 19-20]. Figure (3.1) illustrates the geometry. Figure (3.2) gives a 2-dimensional view of the atom array showing the sharing of electrons in the covalent bonding. This is called intrinsic silicon (no impurities) and the nature of the bonding results in approximately  $5 \times 10^{22}$  atoms/cm<sup>3</sup> [Ref. 19, p. 36-1].

The valence electrons can be in either of two energy states, the conduction band or valence band. An electron in the valence band that is excited by some outside energy source can jump to the conduction band, leaving a vacancy called a hole which results in a positive charge in the bond. Another electron in the valence band can fill this hole, creating another hole in its original position. This repeated process can generate a net movement of electrons in one direction and holes in the opposite direction. This process is called electron-hole generation. In an intrinsic crystal at thermal

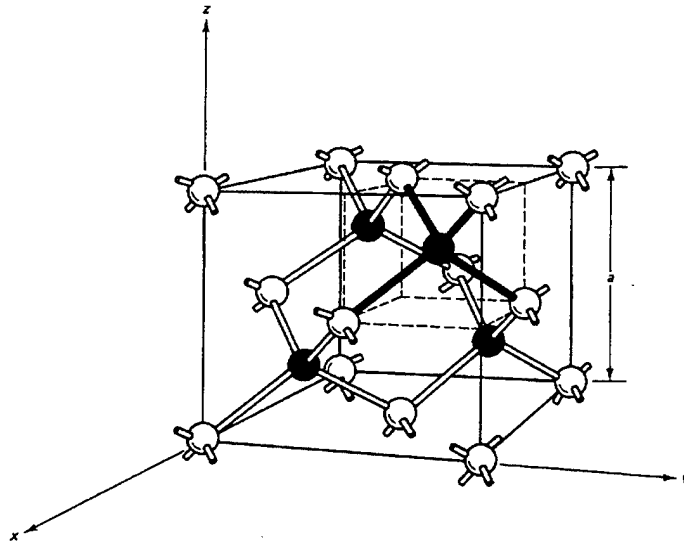


Figure 3.1. Diamond crystal structure. Shaded atoms are of the original face-centered cube. From Ref. [18, p. 8].

equilibrium, the number of holes in the valance band equal the number of electrons in the conduction band. [Ref. 20, p. 9]

Since electrons and holes obey Fermi-Dirac statistics according to quantum theory, the probability that an electron will be in a certain energy state is given by the Fermi-Dirac distribution function:

$$f(E) = \frac{1}{1 + \exp\left(\frac{E - E_f}{kT}\right)} \quad (3.1)$$

where  $f(E)$  is the probability the electron will be in energy state  $E$ ,  $E_f$  is the Fermi energy level at which the electron has a probability of  $\frac{1}{2}$ ,  $k$  is the Boltzman constant ( $8.63 \times 10^{-5}$  eV/°K) and  $T$  is temperature in °K. The density of allowable states per unit volume or number density of states is:

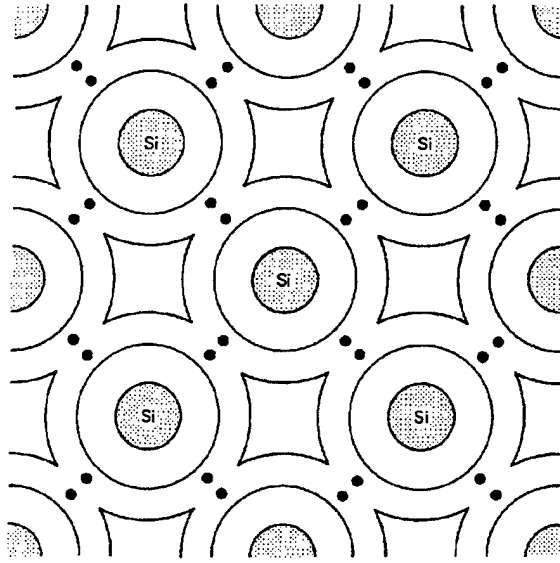


Figure 3.2. Two dimensional version of the silicon lattice illustrating the covalent bonds. The shaded circles represent the Si nucleus the inner two orbitals. The solid circles represent the valence orbitals. Ref. [18, p. 16].

$$N_e(E) = \frac{4\pi (2m_e^*)^{3/2}}{h^3} \sqrt{E - E_c} \quad (3.2)$$

where  $m_e^*$  is the density of states effective mass of an electron in the conduction band and  $E_c$  is the energy at the bottom of the conduction band. The effective mass is an adjustment to the carrier's mass to take into account that the carrier not only experiences force from an external electric field, but also forces from other electrons and atoms within the material. The effective mass is not only material dependent, but also energy band dependent. [Ref. 19, p. 36-3] [Ref. 21, pp. 10-11]

The actual number density of states is given by:

$$n_o = \int_{E_c}^{\infty} N_e(E) f(E) dE \quad (3.3)$$

The upper limit is taken to infinity vice the energy of the upper conduction band because the Fermi-Dirac distribution function contributes little in the upper limit. Normally  $E_c - E_f \gg 3kT$  so that the integral can be evaluated to:

$$n_o = 2 (2\pi m_e^* kT / h^2) \exp(E_f - E_c) / kT \quad (3.4)$$

The result is identical for holes, except that the effective mass for the electrons in the conduction band is replaced for the effective mass of the hole in the valence band and  $E_c$  is replaced with  $E_v$ , the energy at the top of the valence band:

$$p_o = 2 (2\pi m_p^* kT / h^2) \exp(E_f - E_v) / kT \quad (3.5)$$

The only carriers in an intrinsic semiconductor are electrons which are equal to the number of holes. Therefore  $n_o = p_o$  in an intrinsic semiconductor and their product is a constant for a given material at a given temperature. The intrinsic carrier density is given by:

$$n_i^2 = n_o p_o \quad (3.6)$$

The intrinsic carrier density of silicon at room temperature is approximately  $1.4 \times 10^{10}$  carriers/cm<sup>3</sup>. [Ref. 21, pp. 11-12]

The carrier density in intrinsic semiconductors is not high enough for the currents required for proper operation. To increase the carrier density, intrinsic semiconductors are doped (diffused) with impurities. Usually a group V element such as phosphorus or arsenic is used to produce n-type material. Group V element atoms are called donor atoms because four of the five outer electrons form the covalent bonds with the silicon and the fifth electron can be easily

ionized from the donor atom which will add to the intrinsic carrier density. The donor (and acceptor) density,  $N_D$  can vary from  $10^{12}$  atoms/cm<sup>3</sup> to a maximum of about  $10^{20}$  atoms/cm<sup>3</sup> for silicon. This means that for in the lattice structure of the silicon crystal, one silicon atom out of every 500 to  $10^{10}$  is replaced by the donor atom. [Ref. 21, p.12] [Ref. 20, p. 10]

For p-type material, silicon is doped with group III acceptor atoms such as aluminum or boron. The outer shell of these atoms contain three electrons, therefore a hole will be produced when these acceptor atoms removes an electron from the valence band to form the covalent bond in the crystal structure. [Ref. 20, p. 10]

New energy levels are formed just inside the forbidden gap by the introduction of impurities in the semiconductor. In n-type material this energy level is just below the conduction band and for p-type it is just above the valence band. These new energy levels are shown in Figure (3.3).

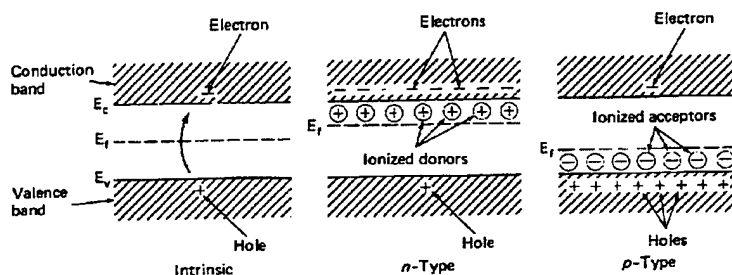


Figure 3.3. Illustration of the shifting of the Fermi energy level due to dopants. From Ref. [21, p. 14].

The existence of these new energy levels bring about a change in the Fermi energy level which is given by:

$$E_f = E_{fi} \pm kT \ln \frac{|N_D - N_A|}{n_i} \quad (3.7)$$

where  $E_{fi}$  is the intrinsic fermi level given by Equations (3.4) and (3.5) and  $N_D$  and  $N_A$  are the donor and acceptor concentrations respectively. It should be noted that since the doped semiconductor is neutral electrically, the following is true:

$$n + N_A = p + N_D \quad (3.8)$$

where  $n$  and  $p$  are the electron and hole carriers respectively. Equation (3.7) makes use of this equation and the assumption that  $|N_D - N_A| \gg n_i$  for n-type material. [Ref. 21, pp. 14-15]

At 300°K the majority of the impurity atoms are ionized, meaning that in n-type material the impurity atoms have given up their electrons and in the p-type material the impurity atoms have taken the electrons from the valence band to complete their covalent bonds in the crystal structure. Since most of the carriers in the doped material are generated by the impurity atoms, the majority carriers (at room temperature) in n-type material are electrons and in p-type material the majority carriers are holes. It should be noted that the impurity ions in both types of semiconductor material are considered to be immobile. Additionally it is assumed that most of the carriers are due to the donor and acceptor atoms and very little contribution is from the intrinsic semiconductor atoms. Table 3.1 summarizes the makeup of the charged particles in an extrinsic semiconductor. [Ref. 22, p. 325]

From the above discussion, it should be clear that  $n \approx N_D$  and  $p \approx N_A$  for n-type and p-type material, respectively. Using



	<i>n</i> -type	<i>p</i> -type
Impurity (dopant) Impurity concentration (cm <sup>-3</sup> )	Donor ( <i>N<sub>D</sub></i> )	Acceptor ( <i>N<sub>A</sub></i> )
Majority carrier Majority carrier concentration (cm <sup>-3</sup> )	Electron ( <i>n<sub>n</sub></i> )	Hole ( <i>p<sub>p</sub></i> )
Minority carrier Minority carrier concentration (cm <sup>-3</sup> )	Hole ( <i>p<sub>n</sub></i> )	Electron ( <i>n<sub>p</sub></i> )
Minority carrier concentration at thermal equilibrium (cm <sup>-3</sup> )	( <i>p<sub>n0</sub></i> )	( <i>n<sub>p0</sub></i> )

Table 3.1. Summary of carriers and impurities. From Ref. [20, p. 11].

this and Equations (3.4) through (3.8), the following can be derived for *n*-type and *p*-type material:

$$n \approx \frac{n_i^2}{N_A}, \quad p \approx \frac{n_i^2}{N_D} \quad (3.9)$$

From both Equations (3.8) and (3.9), it can be seen that

$$n_i^2 = np \quad (3.10)$$

also holds for extrinsic materials. Equation (3.9) is not valid for extremely high doping concentrations that are over 10<sup>18</sup>/cm<sup>-3</sup> or for extreme temperatures. [Ref. 22, p. 335]]

When an electric field  $\bar{E}$  is applied to a semiconductor, the average velocity of an electron,  $v_n$  and the average velocity of a hole,  $v_p$  is given by:

$$v_n = -\frac{e\bar{E}\tau_e}{m_e^*} = -\mu_n\bar{E}, \quad v_p = \frac{e\bar{E}\tau_p}{m_p^*} = \mu_p\bar{E} \quad (3.11)$$

where  $\tau$  is the mean free path between collisions and  $\mu$  is the electron or hole mobility. [Ref. 21, p.17]

Whenever there is a carrier gradient or an electric field, current will exist in a semiconductor. The contribution of total particle current in the semiconductor is from both the holes and electrons flowing in opposite directions. The current density  $\bar{J}$  due to an electric field (drift current of electrons) is then given by:

$$\bar{J} = e(n\mu_n + p\mu_p)\bar{E} \quad (3.12)$$

Since from Maxwell's equations:

$$\bar{J} = \sigma\bar{E} \quad (3.13)$$

where  $\sigma$  is the conductivity, and can be expressed as a function of the material's characteristics: [Ref. 21, pp. 21-23]

$$\sigma = e(n_o\mu_n + p_o\mu_p) \quad (3.14)$$

When excess carriers are introduced in a semiconductor, the carrier density is no longer the equilibrium value. These excess carriers can be generated from external photoexcitation or any ionizing pulses incident on the material. This creates a carrier gradient or a local concentration of charge. These localized concentrations of charge follow Fick's law of diffusion which result in electron and hole particle diffusion current,  $\bar{j}_n$  and  $\bar{j}_p$  respectively:

$$\bar{j}_n = -e(-D_n\nabla n), \quad \bar{j}_p = e(-D_p\nabla p) \quad (3.15)$$

where  $D_{n,p}$  is the diffusion coefficient for electrons and holes in silicon. Then the total particle current due to diffusion and any electric field present is:

$$\bar{J}_n = e(n\mu_n\bar{E} + D_n\nabla n + p\mu_p\bar{E} - D_p\nabla p) \quad (3.16)$$

Utilizing charged particle transport theory, the kinetic theory of gases and the definition of mobility (Equation

3.11), the following Einstein relations can be derived: [Ref. 21, pp. 22-23]

$$\frac{D_n}{\mu_n} = \frac{D_p}{\mu_p} = kT/e \quad (3.17)$$

Thermal carriers are produced when an electron in the valence band is thermally excited to the conduction band. This transition can take place in a single step (band-to-band) or through an intermediate band located in the forbidden band (this band is caused by the semiconductor impurities as discussed earlier). The latter process is most probable in silicon material. The rate of carrier generation can be seen to be proportional to the number of defects in the material. [Ref. 20, pp. 22-23]

In order to maintain equilibrium carrier density in the material, a process called carrier recombination takes place. Like carrier generation, recombination is a two-step process in silicon like carrier combination. This process involves an electron in the conduction band combining with a hole in the valence band, hence destroying a hole-electron pair. A photon is released and in order to conserve both momentum and energy, a particle called a phonon is released (Refer to Figure 3.4). The phonon is analogous to the photon, but is associated with the acoustic waves of the vibrating lattice. Sometimes instead of photon emission, the energy is transferred to another electron as kinetic energy. This is known as an Auger process. In thermal equilibrium, the recombination rate and thermal generation rate are equal in order to maintain equilibrium charge density. [Ref. 21, pp.23-27]

As mentioned before, the impurities in the semiconductor give rise to energy levels in the forbidden zone. This results in traps or recombination centers, where an electron can be captured or trapped and held by the impurity atom. If the energy level of the impurity atom has a high probability

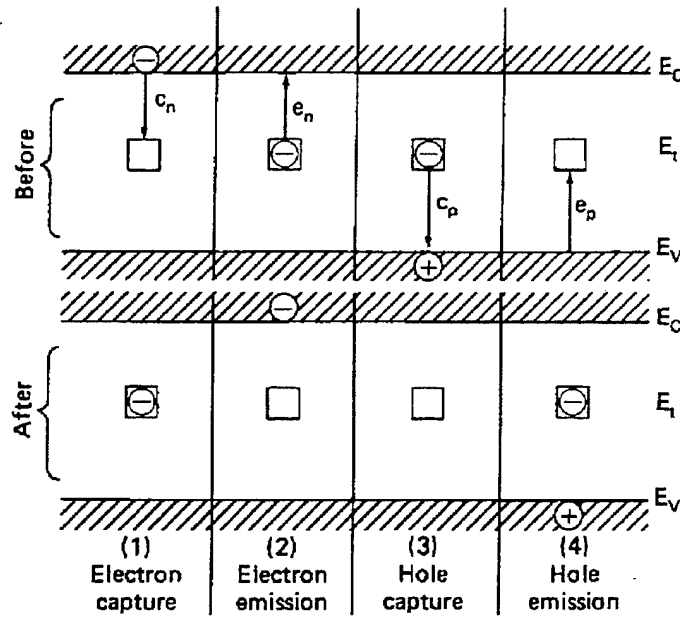


Figure 3.4. Carrier generation and recombination. From Ref[21, p. 24].

of reemitting the electron before it recombines with a hole, then this energy level is called a trap. This is the case if this impurity energy level is close to the conduction band. On the other hand, if the impurity energy level is midway in the conduction-valence energy gap, it is probable that the electron will recombine before it is reemitted. In this case it is termed a recombination center. [Ref. 21, p. 25]

The average time an electron spends in the conduction band or hole in the valence band before recombination is called average or mean carrier lifetime,  $\tau$ . At equilibrium, it can be seen that:

$$g_{on} = \frac{n_o}{\tau_{no}} = \frac{p_o}{\tau_{po}} = g_{op} \quad (3.18)$$

where  $\tau_{no}$  and  $\tau_{po}$  are the average lifetimes for electrons and holes and  $g_{on}$  and  $g_{op}$  are the thermal equilibrium generation

rates. Under non-equilibrium states, generation and combination rates are not necessarily equal: [Ref. 21, p. 27]

$$g_n = g_p, \quad \frac{n}{\tau_n} = \frac{p}{\tau_p} \quad (3.19)$$

The concept of generation and recombination leads to definition of the carrier lifetime: "the average length of time that the charge carriers exist between the time that they are generated and the time that they recombine." [Ref. 23, p. 105] The minority carrier lifetime,  $\tau_e$  and  $\tau_p$  for electrons and holes respectively, can be expressed quantitatively by the following equation:

$$\tau_e = \frac{1}{c_n N_t}, \quad \tau_p = \frac{1}{c_p N_t} \quad (3.20)$$

where  $c_n$  and  $c_p$  are the electron and hole capture crosssections. [Ref. 19, p. 36-17]

When the thermal equilibrium carrier densities are altered by some outside energy source, excess carriers are introduced into the semiconductor. This is called carrier injection. When the excess carrier concentration is less than that in thermal equilibrium, it is referred to as low-level excess carrier injection. High level carrier injection refers to carrier concentrations higher than the equilibrium concentration. [Ref. 22, p. 341]

### C. FORMATION AND CHARACTERISTICS OF A PN JUNCTION

When n-type and p-type materials are joined together, electrons from the n-side diffuse to the p-side and holes from the p-side diffuse to the n-side. This forms what is called as a depletion or space charge region in the vicinity of the junction. There are positive ions on the n-side and negative ions on the p-side. This results in a built-in electric field across the region. The width of this depletion layer for an

applied voltage,  $V_o$  is given by:

$$I = [2\epsilon\epsilon_o(\phi_o - V_o)(N_A^{-1} + N_D^{-1})/e]^{1/2} \quad (3.21)$$

where  $\phi_o$  is the electrostatic potential between the two regions. Figure (3.5) illustrates the formation of the space depletion region. [Ref. 24, pp. 39-48]

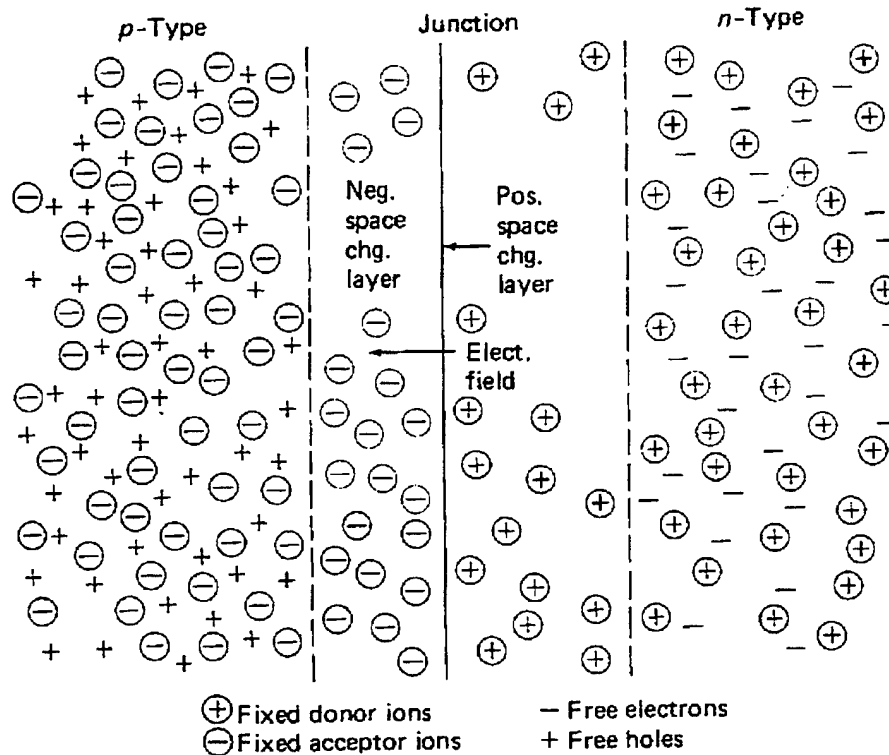


Figure 3.5. Formation of the space charge (depletion) region in a pn junction. From Ref [21, p. 71].

Since there is a volume surrounded with opposite charge, a junction capacitance is generated. Because the capacitance, depends on the junction width, it is dependent on the applied

voltage,  $V_o$  as in the following relationship: [Ref. 21, p.79]

$$C_j = \left( \frac{e\epsilon\epsilon_o}{2(1/N_A + 1/N_D)(\phi_o - V_o)} \right)^{1/2} \quad (3.22)$$

When a junction is forward biased, the minority carriers are reorganized outside the depletion layer. This results in diffusion capacitance:

$$C_d = \frac{e^2}{kT} (L_n p_{0n} + L_p n_{p0}) \exp\left(\frac{eV_o}{kT}\right) \quad (3.23)$$

Diffusion capacitance can be related to minority carrier lifetime by: [Ref. 21, p. 80]

$$C_d = (e/kT) I\tau \quad (3.24)$$

The bipolar junction transistor (BJT) is formed with two pn junctions as shown in Figure (3.6). The BJT consists of three parts: the base, emitter and collector. Generally the emitter is more heavily doped than the base to increase the transistor current gain, as will be shown later. For operation in the active region (for use as an amplifier), the base-emitter junction is forward biased and the collector-base junction is reversed biased.

In the active region of an npn BJT, the emitter-base current is primarily a result of the emitter injecting (or emitting) electrons into the base. The electrons, now minority carrier, diffuse through the base and flow into the reversed bias collector-base depletion region. Due to finite basewidth some electrons in the base will recombine with the holes in the base (assuming the basewidth is too narrow for recombination to occur). The electrons flow into the collector (positive with respect to the base), where they appear as drift current. The collector current can be shown to be proportional to  $\exp(eV_{BE}/kT)$  and is given by:

$$I_C = I_s \exp(eV_{BE}/kT) \quad (3.25)$$

where  $V_{BE}$  is the base-emitter voltage and  $I_s$  is the saturation current. This shows that small fluctuations in the base voltage result in large fluctuations in the collector current, hence current amplification. This current amplification or gain is given as the ratio of the collector and base currents,  $\beta = I_C/I_B$ . Figure (3.6) shows the flow of currents in a npn BJT biased in the active mode. [Ref. 25, p. 196]

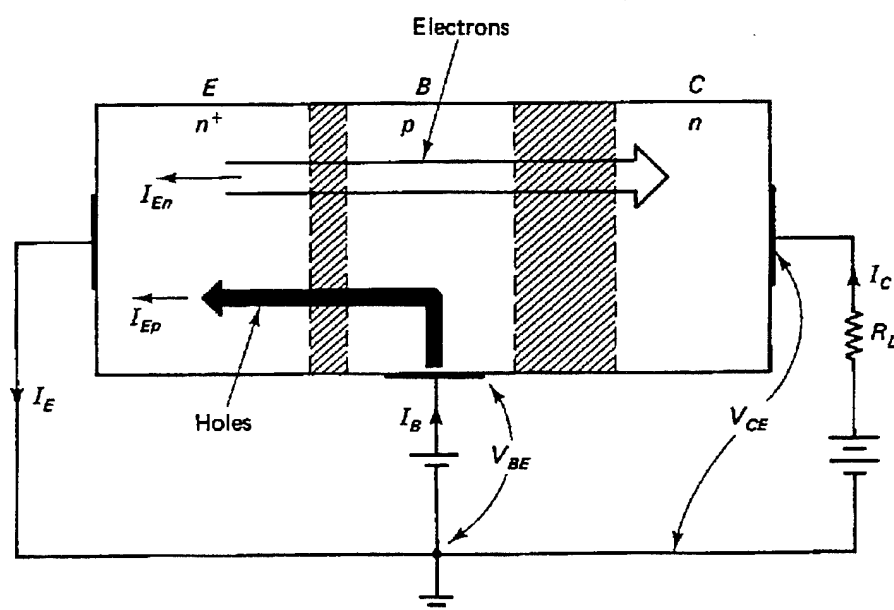


Figure 3.6. Flow of currents in a NPN transistor biased for active operation. From Ref [18, p. 339].

#### D. RADIATION EFFECTS IN A BIPOLAR TRANSISTOR

The two basic effects of radiation on semiconductor material are injection of carriers due to ionization and displacement of atoms in the lattice structure [Ref. 2, p. 1512]. The first of these, ionization, is most important for



this research, since with electron bombardment, ionization is the primary source of radiation damage.

Ionization is the result of high energy photons interacting with the semiconductor and producing charged particles. The primary photocurrent will increase the base current resulting in a secondary photocurrent in the collector. The photoelectric effect, Compton scattering and pair production, described in Chapter II are included in the ionization processes discussed here. In turn, these charged particles generate photocurrents. Enhancement of bulk conductivity is a major effect of ionization and it is given by: [Ref. 21, p. 22]

$$\delta\sigma = e(\mu_n\delta n + \mu_p\delta p) \quad (3.26)$$

where  $\delta\sigma$  is the difference between the post and pre-radiation values of conductivity, and  $\delta p, n$  are the excess carrier concentrations.

Because BJT current gain is so important in analog networks (especially amplifier circuits), its change due to the radiation effect on it is of great concern. Current gain degradation can be the dominant effect in many bipolar transistors [Ref. 26, p. 2027]. A major cause of current gain degradation is the increase of surface states at the oxide-silicon interfaces. This in turn increases the surface recombination velocity,  $S_p$ .  $S_p$  is a measure of the tendency of carriers to drift toward the surface and recombine. This increase in  $S_p$  results in a decrease in current gain  $\beta$  which can be seen from the following equation for  $\beta$  as a function of the transistor's physical characteristics: [Ref. 27, p. 567]

$$1/\beta = S_p A_s W / D_b A_e + \sigma_b W / \sigma_e L_e + \frac{1}{2} (W/L_b)^2 \quad (3.27)$$

where:  $S_p$  is the recombination velocity

$A_s$  is the area for recombination

$W$  is the base width

$D_b$  is the base diffusion constant

$A_e$  is the emitter area

$L$  is the diffusion length

$\sigma_{b,e}$  is the conductivity of base and emitter

The first term is due to surface recombination, the second is due to emitter efficiency and the third is due to volume recombination.

Ionization can also cause high-injection level minority current into the base side of the base-collector region resulting in less exposed space charge from the base and more space charge on the collector side. This results in an expansion of the effective base width, and hence a decrease in  $\beta$  as reflected in the above equation. An increased base width also results in increased base transit time which decreases the transition frequency,  $f_T$ . [Ref. 21, p. 108]

#### IV. EXPERIMENTAL APPROACH

##### A. OVERVIEW OF THE NPS LINAC

This research utilized the 110 MeV NPS linear accelerator (LINAC) to simulate the total dose ionization effects on a device. The LINAC consists of three ten-foot accelerating sections, each powered by a 22 megawatt (peak) klystron amplifier. An electron gun injects 80 keV electrons into the accelerator. The three klystrons modulate the electrons in "bunches" or packets. The klystrons are controlled by a master RF oscillator which turns on the beam voltage to the klystrons. The klystrons are driven by a tunable magnetron at 2.856 GHz and at 6 kilowatts (peak). Since, at 80 keV the electrons are travelling about half the speed of light, those electrons not travelling at the same speed are lost. The number of electrons lost is reduced by inserting a "prebuncher" in the accelerator with a net result of reducing the spacial distribution of the electrons into a smaller bunch. The frequency of the electron beam is 60Hz with a pulse width of about 3.5 microseconds. Figure (4.1) gives an overview of the LINAC's major components and spatial layout.

At the end of the third section of the accelerator is a collimator which provides a "source point" for the deflection magnet and quadrapole lenses. The deflection magnet separates the various energies in the beam, so that the desired energy can be selected by the energy defining slits. This magnet also serves to deflect, as the name implies, the electron beam so that the counting equipment is not in line with the undesirable forward radiation of the electrons.

In order to measure the fluence (total number of electrons per unit area) of the electron beam, a secondary emission monitor (SEM) is utilized. This is located at the end of the target chamber of the LINAC. The electron beam passing through the SEM causes charge to accumulate on a

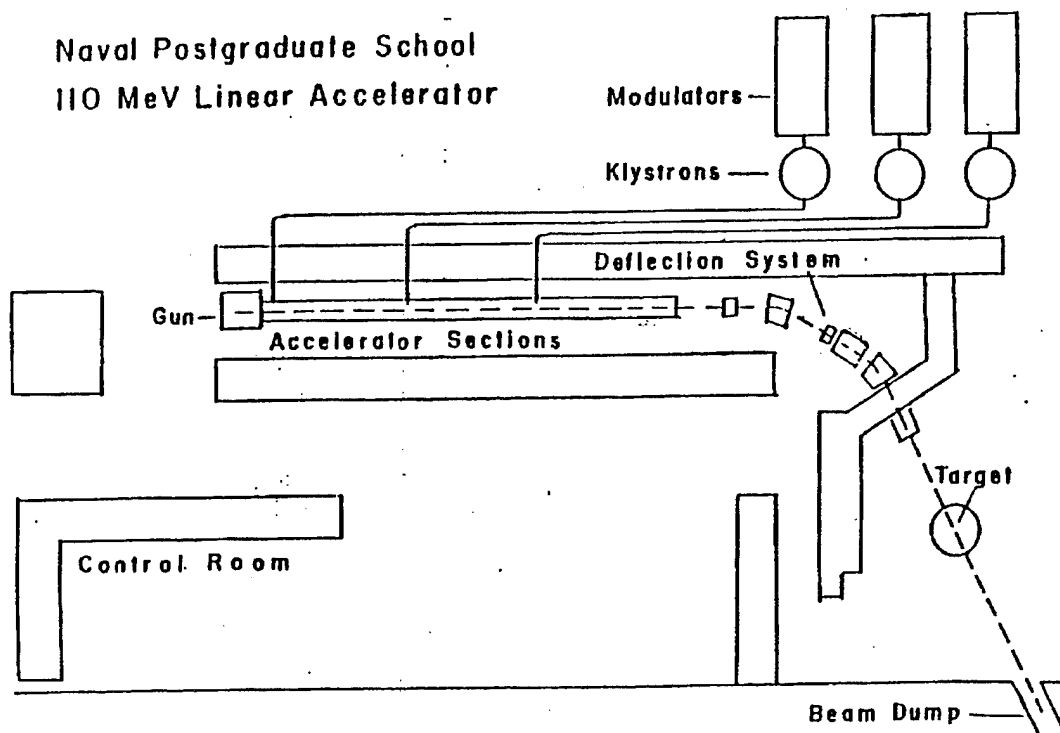


Figure 4.1. Spatial layout and major components of the NPS linear accelerator. From Ref. [28, p. 73].

capacitor which is remotely connected to a voltage integrator in the control room. The accumulated charge  $Q$ , due to  $N$  electrons of charge  $e$ , on the SEM is given by:

$$Q = Ne = CV \quad (4.1)$$

[Ref. 29, pp. 20-23] [Ref. 30, pp. 7-8] [Ref. 31, p. 41-43]

## B. DOSIMETRY

### 1. Overview

Now that we have a radiation source, the problem arises on how to measure the radiation absorbed by the target device. There are many different methods of determining dose along with a variety of materials to accomplish this measurement. Among some types of dosimetry systems are: calorimeters,

films, cobalt glass, Victoreen thimble-ionization chambers, thermoluminescent dosimeters (TLD's), to name a few. Selection of the right dosimetry system is dependent on the type of radiation testing done (i.e. ionizing, displacement damage), the radiation source and the target material (silicon in the case of this research). [Ref. 7, p. 87]

Before going on to explain the method of dosimetry used in this research, a few terms relating to dose must be defined. First, is absorbed dose or total dose. This is the mean energy absorbed per unit mass of irradiated material and is given by  $D$  in the following equation: [Ref. 32, p. I-3]

$$D = \Delta E_D / \Delta m \quad (4.2)$$

where  $\Delta E_D$  is the energy absorbed by the material. Dose is given in rads (radiation absorbed dose), where one rad is defined as 100 ergs of energy absorbed per gram of material.

Particle fluence,  $\phi$  is the number of particles,  $N$  incident on a cross-sectional area. Energy fluence,  $\psi$  is the radiant energy incident on a cross-sectional area. These two parameters are given by: [Ref. 32, p. I-7]

$$\phi = dN/dA, \quad \psi = dE/dA \quad (4.3)$$

Another term of great importance in dosimetry, is charged particle equilibrium (CPE). CPE is said to exist if the total energy carried out of a material by charged particles is equal to the energy carried into the material by charged particles. In the case of a photon beam incident on a material, CPE exists when the thickness of the material is approximately equal to the range of the most energetic secondary electron. This is sometimes referred to as the equilibrium thickness. Using this concept of CPE, the following equation can be derived:

$$\frac{D_1}{D_2} = \frac{(\mu_{en}/\rho)_{E,1}}{(\mu_{en}/\rho)_{E,2}} \quad (4.4)$$

where  $(\mu_{en}/\rho)_{E,Z}$  is the mass energy absorption coefficient at a photon fluence of energy  $E$  and material  $Z$ .  $D_Z$  is the absorbed dose of material  $Z$ . This equation assumes a monochromatic photon beam and little interference with surrounding material. [Ref. 33, p. 1171]

Unfortunately, the concept of CPE is not valid in an electron beam environment. But a similar relationship can be derived for electron beams at high energies ( $E > 12$  MeV), assuming that electrons interacting with the material will deposit energy within the material:

$$\frac{D_1}{D_2} = \frac{(S_{col}/\rho)_{E,1}}{(S_{col}/\rho)_{E,2}} \quad (4.5)$$

where  $S_{col}/\rho$  is the mass collision stopping power expressed in MeV·cm<sup>2</sup>/g. Additionally, the assumption is made that the material is thin enough to ignore any bremsstrahlung absorption. [Ref. 33, p. 1172]

## 2. Application of TLD Dosimetry

In this research, manganese-doped calcium fluoride (CaF<sub>2</sub>:Mn) was used for dosimetry measurements. This is a synthetic material. Naturally occurring deposits of fluorite cannot be used because it displays non-reproducible light output and glow curves. This material is available in many physical forms and packaging. The type used here were 1/8 x 1/8 x 0.035 inch chips. [Ref. 34, p. 3-9]

When CaF<sub>2</sub> is exposed to radiation, holes and electrons are introduced and trapped by the metastable energy levels or traps in the forbidden gap (formed by the introduction of manganese). The density of the filled traps is proportional

to the total dose absorbed. To measure this absorbed dose, the TLD is then removed from the radiation source and heated in the TLD reader chamber. This heating gives the electrons in the traps enough energy to be released and combine with free holes, thus emitting light. The intensity of this light is proportional to the density of filled traps which in turn, is proportional to the total dose. [Ref. 32, p. I-13]

There are two major reasons for choosing this type of dosimetry. First, because of its linearity up to 100 krad, dosimetry calculations become very simple. Second, the energy dependence of unshielded  $\text{CaF}_2$  is low at energies greater than one MeV. At energies less than this (not applicable in this research), the TLD can be surrounded by a thick and thin metallic shield to flatten the energy dependence at energies below one MeV where error can be limited to 20% at energies greater than 80 keV. Figure (4.2) illustrates this energy dependence. [Ref. 34, p. 3-14]

At high energies, the absorbed dose for  $\text{CaF}_2$  can be considered equivalent to that of silicon. However, for energies less than about 12 MeV, Equation (3.4) must be used to find the equivalent silicon dose, given the  $\text{CaF}_2$  dose. The energy absorption of TLD's and aluminum is plotted in Figure (4.3). Note that at 10 MeV (right boundary of the figure), the energy absorption for silicon and  $\text{CaF}_2$  are almost identical. [Ref. 34, p. 1172]

In conducting our dosimetry calibrations, the TLD chip was placed next to a "dummy" device under test (an identical device to the one actually irradiated). This ensured that the calibration was done at the precise location of the device under test. The ideal situation would be to have the TLD placed inside the packaging material of the "dummy" chip and then pull it out after irradiation to measure the absorbed dose. This was obviously impractical for our setup, therefore the former method had to be used.

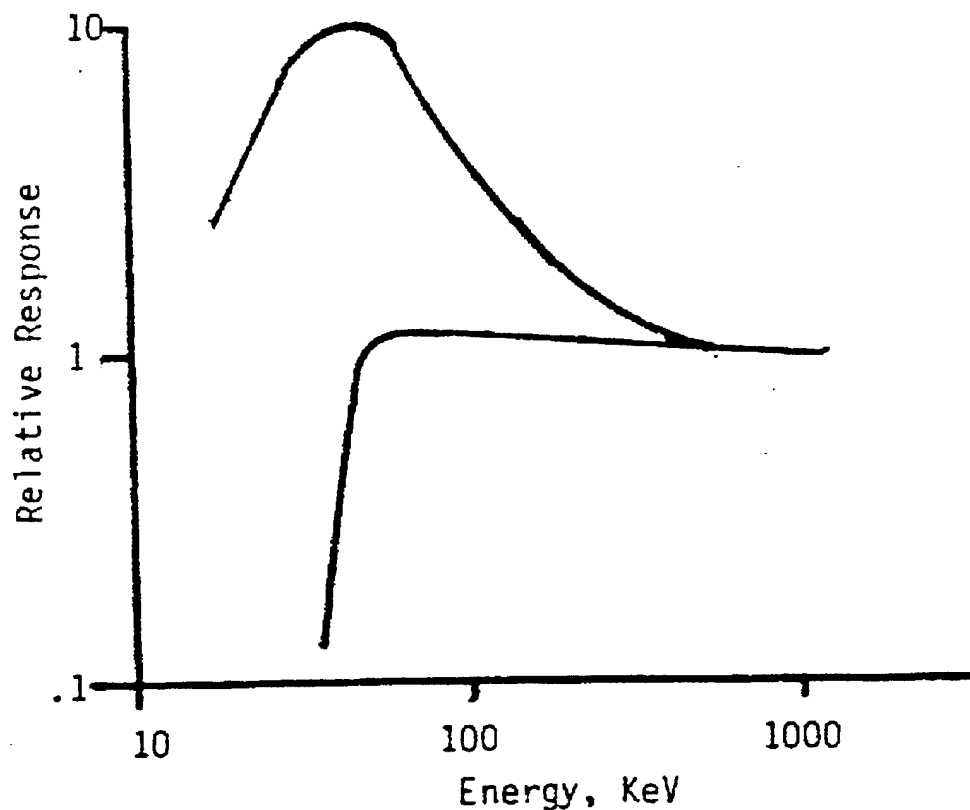


Figure 4.2. Energy dependence of CaF<sub>2</sub>:Mn. The top curve is the response for unshielded CaF<sub>2</sub>:Mn. The bottom curve is for shielded CaF<sub>2</sub>:Mn. From Ref [34, p. 3-14].

Once the TLD was in place, the LINAC was pulsed (the beam was tuned and focused prior to this) for a predetermined amount of accumulated charge on the SEM, corresponding to a predetermined voltage on the capacitor. The TLD is removed and the total dose accumulated is measured. Several runs are made at various capacitor voltage levels. Since the SEM is known to be linear, the results of total dose vs. capacitor voltage can then be plotted and extrapolated to get a value for Mrads per total voltage on the capacitor. Note that since the TLD's utilized, saturate at approximately 10 krad, the



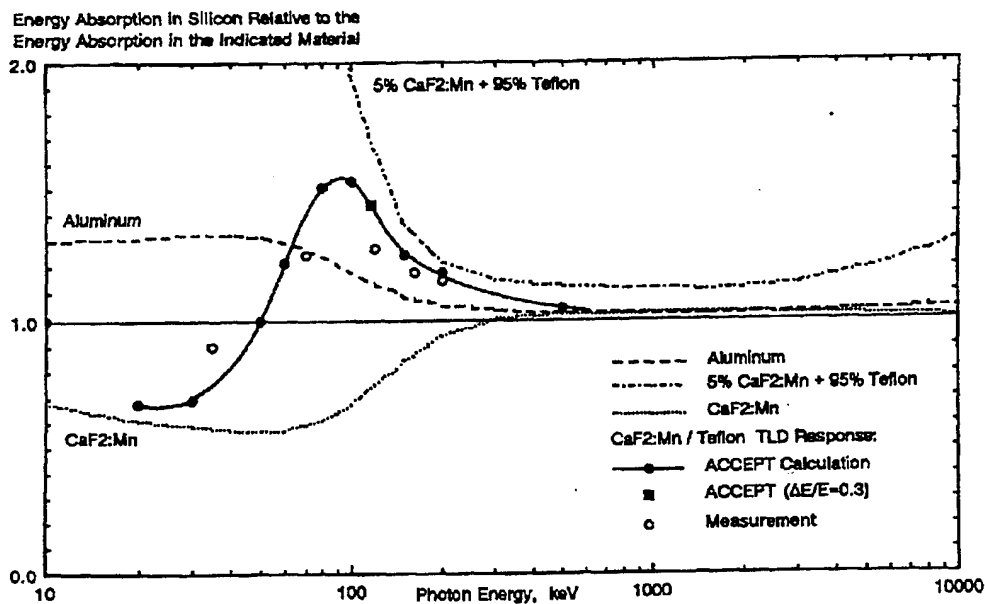


Figure 4.3. Energy dependence of various materials relative to silicon. From Ref [35, p. 1755].

irradiation time for the TLD's is on the order of seconds. According to simulations using CEPXS/ONELD radiation transport code to model the TLD response, the worst case deviation in total dose (Si) measurement may only be 15% at 60 MeV. This deviation is due to the differences in surrounding material in the case of the TLD chip and the silicon die. The actual experimental dosimetry plots are shown in the next chapter. [Ref. 33, p. 1174]

### C. DESCRIPTION OF THE DEVICE UNDER TEST

The devices used for studying the total dose effects were Harris UHF-1 bipolar, 40 pin side brazed DIPs with gold plated kovar lids braze sealed. Each chip contained 13 NPN transistors of various emitter sizes.

The UHF-1 process is a dielectric isolated, wafer bonding process that utilizes Silicon-On-Insulator (SOI) technology and vertical trenches. This technology reduces collector-base capacitance by forming a buried layer and contact and a recessed oxide region. The bonded wafer oxide allows for vertical inter-device isolation. Figure (4.4) reveals the cross section of the UHF-1 architecture. Typical parameter values are shown for both the NPN and PNP transistors in Table 4.1. [Ref. 36, p. 260-261] [Ref. 37, p. 37-42]

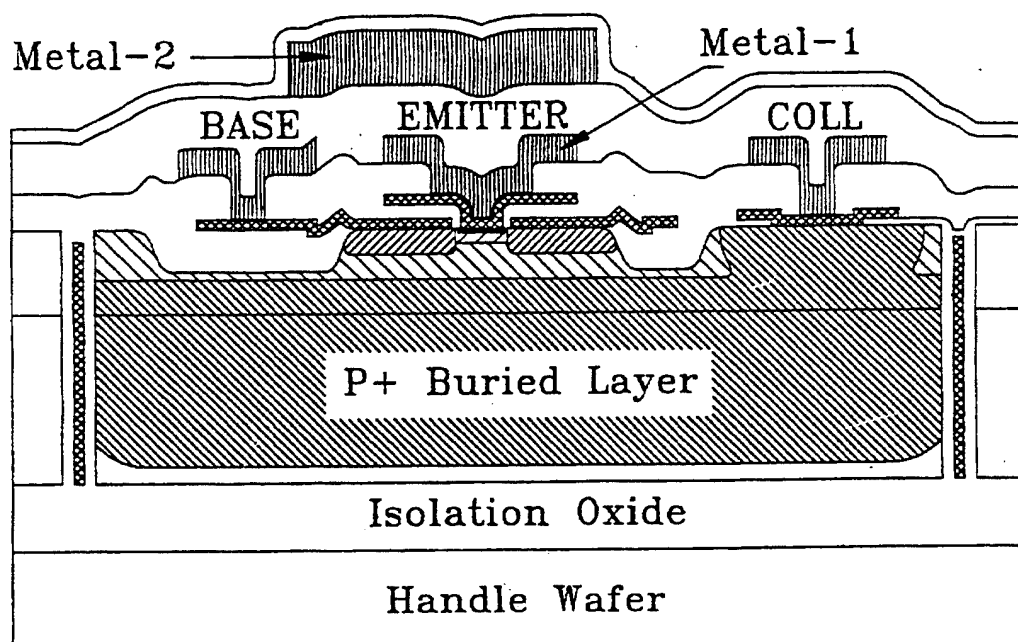


Figure 4.4. Cross section of the UHF-1 architecture. From Ref [36, p. 261].

#### D. CIRCUIT DESIGN

The 13 transistors were utilized for 3 separate sets of measurements. Nine of the transistors were utilized to construct a simple operation amplifier in a closed loop configuration. The  $I_C$  vs.  $V_{CE}$  family of curves for different

PARAMETER	DEFINITION	NPN	PNP	UNITS
Beta	DC Current Gain	100	40	-
V <sub>a</sub>	Early Voltage	60	20	V
BV <sub>EB0</sub>	-	5.5 MIN	4.5 MIN	V
BV <sub>CE0</sub>	-	12 MIN	12 MIN	
BV <sub>CE0</sub>	-	8 MIN	12 MIN	V
R <sub>bx</sub>	Extrinsic Base Resistance	40	25	Ohms
R <sub>bi</sub>	Zero Bias Intrinsic Base Resistance	350	180	Ohms
R <sub>cx</sub>	Parasitic Collector Resistance	35	50	Ohms
R <sub>ci</sub>	Intrinsic Collector Resistance	225	225	Ohms
C <sub>ic</sub>	Zero Bias Collector-Base Capacitance	60	80	fF
C <sub>cs</sub>	Collector-Substrate Capacitance	30	30	fF
f <sub>T</sub>	Transition Frequency	9	5.5	GHz

Table 4.1. Typical parameters for UHF-1 transistor. From Ref. [36, p.263].

values of  $I_B$  were monitored to extract current gain measurements of three transistors. The remaining transistor was used in a common emitter configuration for measuring the base and collector small signal currents as a function of frequency. These currents were used to calculate the transition frequency,  $f_T$ .

### 1. Design of the Operational Amplifier

The obstacle in designing an operational amplifier was the restriction to 9 NPN transistors and no PNP's. Additionally, the biasing of the transistors had to be calculated very carefully since these transistors had very low current ratings (the maximum current rating or power dissipation is not known). After some trial and error and destruction of transistors a suitable opamp design was found. Circuit simulation using PSpice was used extensively to model these transistors based on the specification sheet from Harris and experimental measurements. These transistor models in turn, were then used to design the opamp. The final design is shown in Figure (4.5) and its resulting phase plot and

frequency response in a closed loop configuration are shown in Figures (4.6) and (4.7). It was designed to have approximately a 1.5MHz gain-bandwidth product.

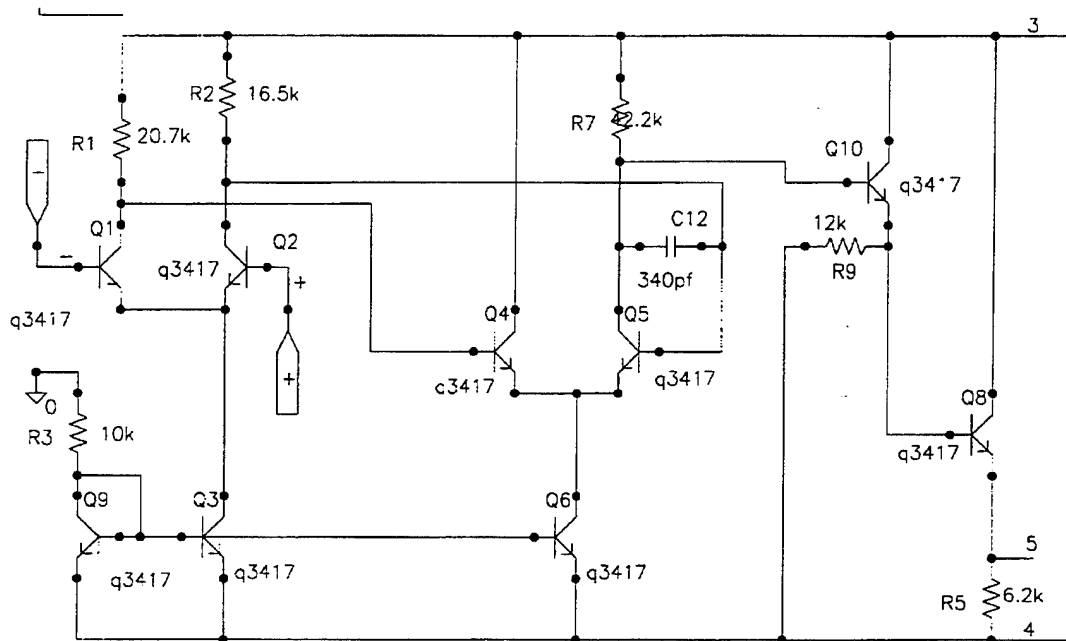


Figure 4.5. Operation amplifier design used for radiation testing.

## 2. Common Emitter Circuit

One way to experimentally determine the transistor transition frequency is to measure the ratio of the collector and the base small signal currents as a function of frequency. This was accomplished by building a common emitter circuit as shown in Figure (4.8).

If  $R_B$  is large and  $R_L$  is small compared to  $R_C$  then the collector and base currents are given as follows:

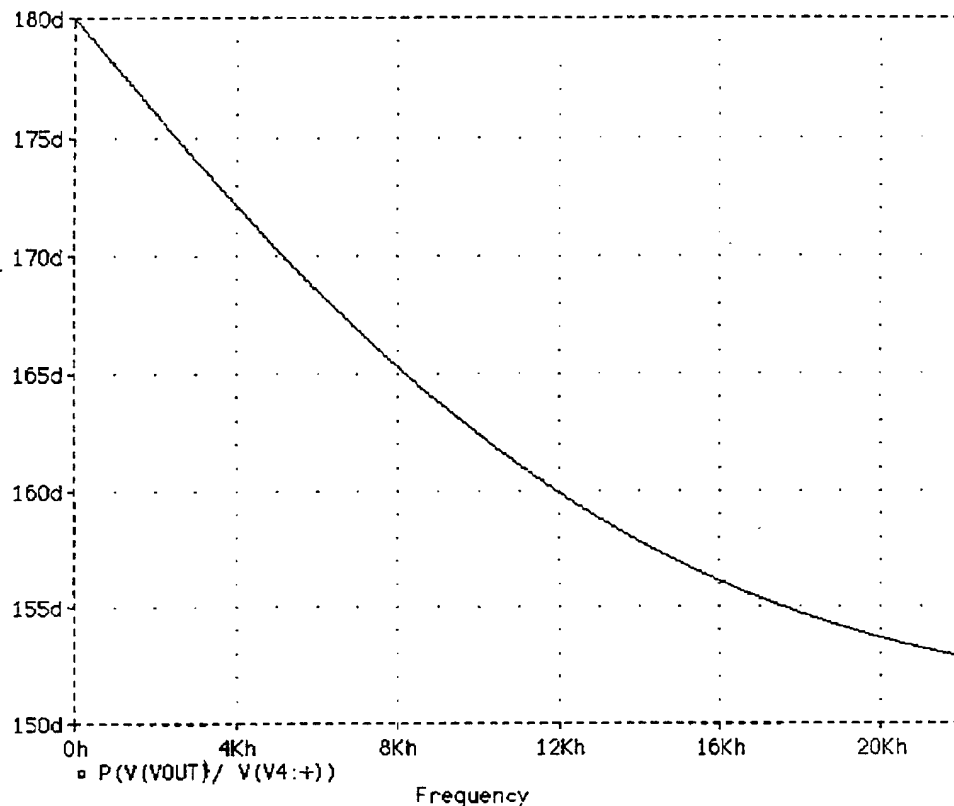


Figure 4.6. Phase plot of opamp.

$$i_c \approx i_o = -\frac{V_o}{R_L}, \quad i_b \approx i_i = \frac{V}{R_s} \quad (4.6)$$

A small signal of 10 mV<sub>p</sub> can be injected into this circuit at varying frequencies and the small signal base and currents can be measured. Then the AC  $\beta$  or  $\beta_{ac}$  can be calculated from:

$$h_{fe} = \frac{i_c}{i_b} \quad (4.7)$$

and a plot for  $h_{fe}$  as a function of frequency can determine  $f_T$ . The value of  $f_T$  can now be used to find the sum of the parasitic capacitances  $C_\mu$  and  $C_\pi$  in the high frequency hybrid-

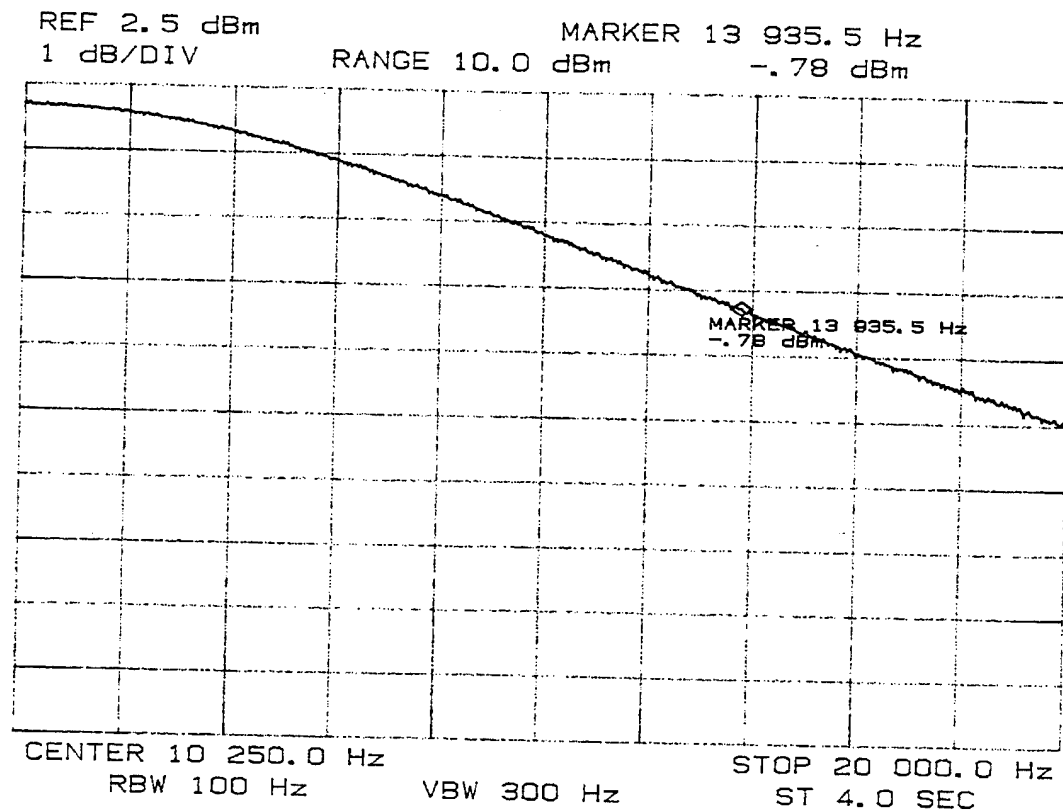


Figure 4.7. Opamp closed loop response.

$\pi$  model: [Ref. 25, p. 526]

$$f_T = \frac{I_C / V_T}{2\pi (C_\pi + C_\mu)} \quad (4.8)$$

$C_\mu$  is the collector-base capacitance and  $C_\pi$  is the emitter-base capacitance.

### 3. Measurement of DC Current Gain ( $\beta$ )

A Tektronics 576 curve tracer was utilized to display the  $I_C$  vs.  $V_{CE}$  family of curves. The DC current gain,  $\beta$  was found for a given  $I_B$  at a given  $V_{CE}$  by the following definition:

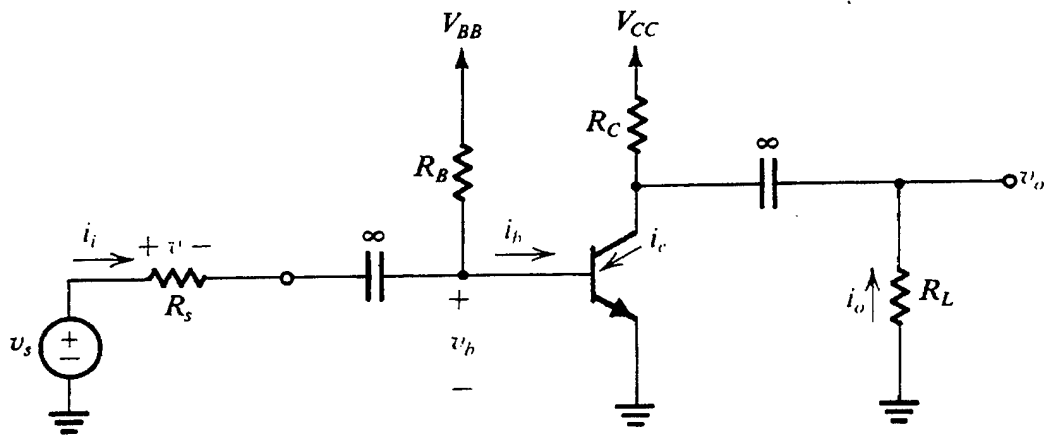


Figure 4.8. Common emitter circuit used in experimental setup. From Ref. [25, p. 522].

$$\beta = \frac{I_C}{I_B} \quad (4.9)$$

While this measurement is very straightforward, the problem of noise had to be dealt with since the device and the curve tracer were connected together by over 80 ft of cable. The method used to deal with the noise is explained in the next section.

#### E. EXPERIMENTAL SETUP

The three circuits just described were implemented on a printed circuit board. With the exception of the common emitter circuit, all measurements had to be made in the LINAC control room which was approximately 80 ft away from the target device. This introduced an obvious noise problem. Since noise was a significant factor, all inputs and outputs to the circuit board were required to be connected with coaxial cables right up to the board connection. All the coaxial cables between the control room and the device were

triple shielded and ran through a steel conduit for most of the length. A setup of the circuit board is shown in Figure (4.9).

An AC small signal voltage (5-10 mV<sub>pp</sub>) was required for both the common emitter and the operational amplifier circuits. The signal source for both of these circuits was the output of the tracking generator of a Hewlett Packard 3585B spectrum analyzer. This tracking generator had an option to manually sweep the frequency, which was ideal for the common emitter circuit measurement of  $i_c$  and  $i_e$  as a function of frequency. In the continuous sweep mode, the signal generator was used to display the closed loop frequency response of the opamp.

The tracking generator output level was set to its maximum level of 1.1V<sub>pp</sub>, to minimize noise interference with the signal. Of course it was necessary to step down the voltage for the opamp and common emitter circuits. This was done on the board utilizing the opamps to reduce the voltage to the 10 mV<sub>pp</sub> range. This worked extremely well as can be seen by the closed loop response of the opamp in the next chapter. This is the display that was present while the LINAC klystrons were on (the klystrons were the most significant noise source in the LINAC environment). An oscilloscope was used to remotely measure the opamp slew rate.

Because of the small amplitude of the voltages that were measured in the common emitter circuit, auto-ranging voltmeters were setup near the target device. The voltmeters were read remotely in the control room via closed circuit video cameras. Figure (4.10) illustrates this setup.

As stated previously, two Tektronics curve tracers were utilized to obtain current gain (refer to Figure (4.11)). With some experimentation it was found that negligible noise was observed on the curve tracer display if the inner conductor of the coaxial cable was used for the stepped base



current. The emitter (grounded at the curve tracer) was placed on the outer conductor of the coaxial cable. The collector current was place on a single conductor cable. This arrangement produced the optimum display on the CRT. There was negligible difference between the remote curve tracer measurements and local curve tracer measurements. The quality of the traces can be seen in Figure (4.12).

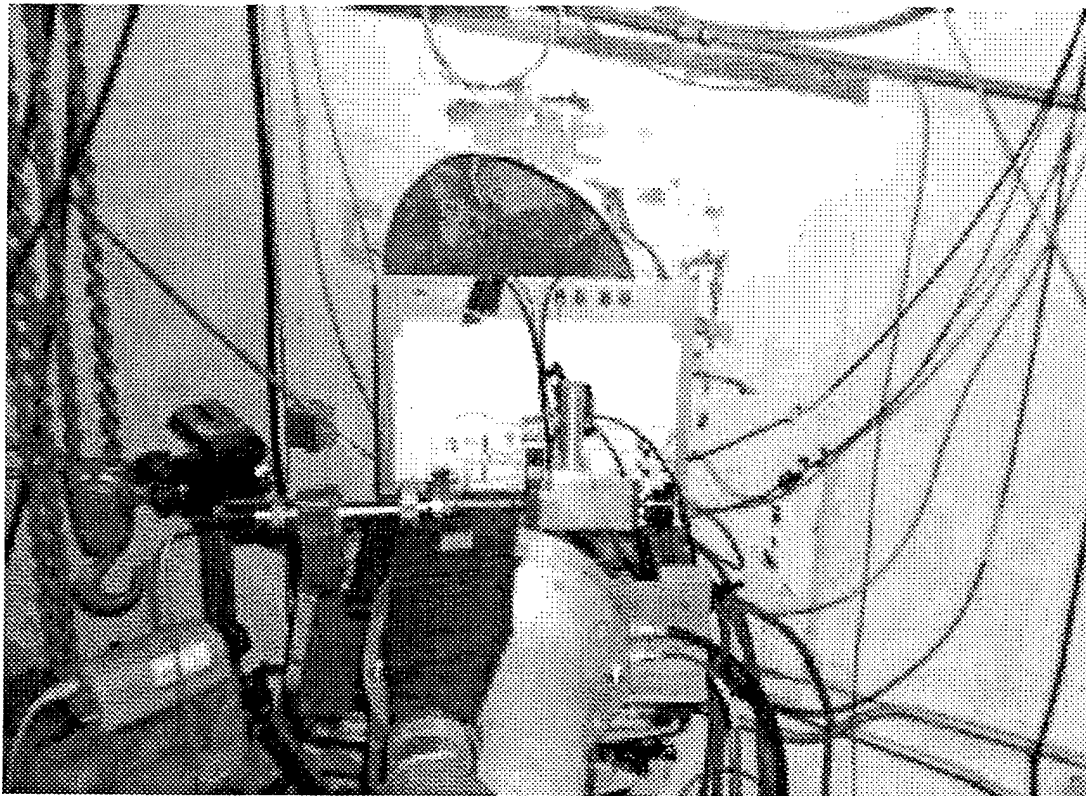


Figure 4.9. Setup of circuit board in the target area of the LINAC.

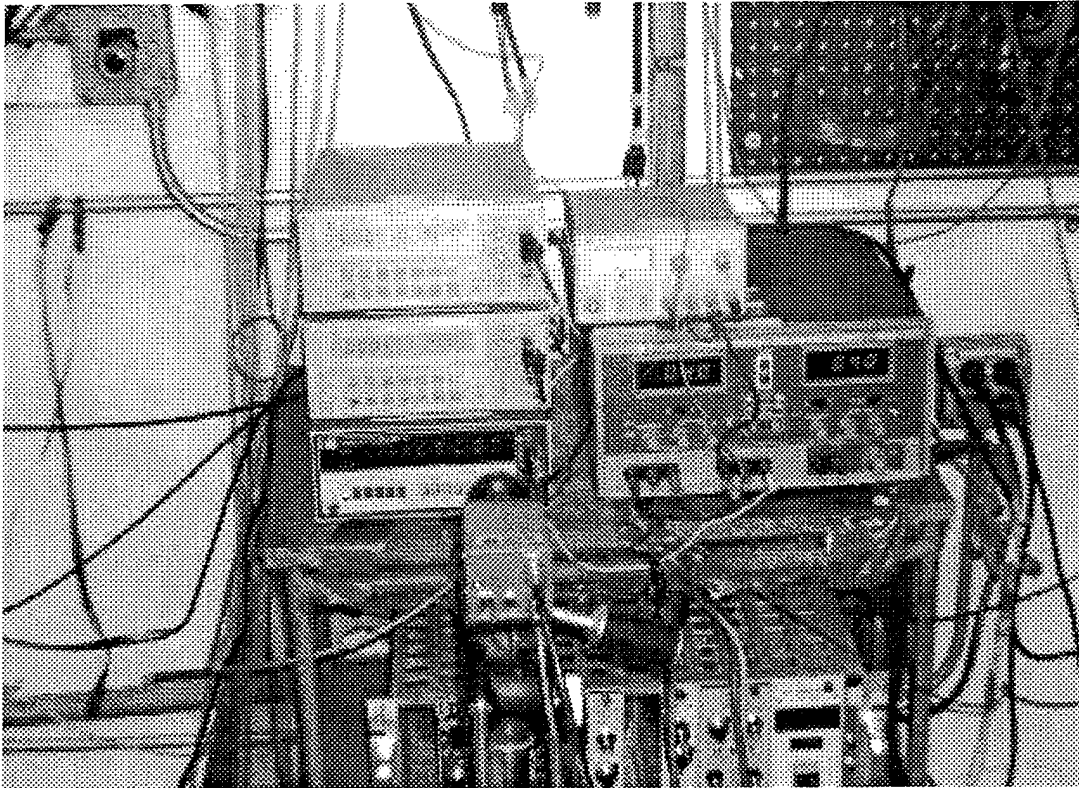


Figure 4.10. Setup of the voltmeters for measurment of common emitter circuit.

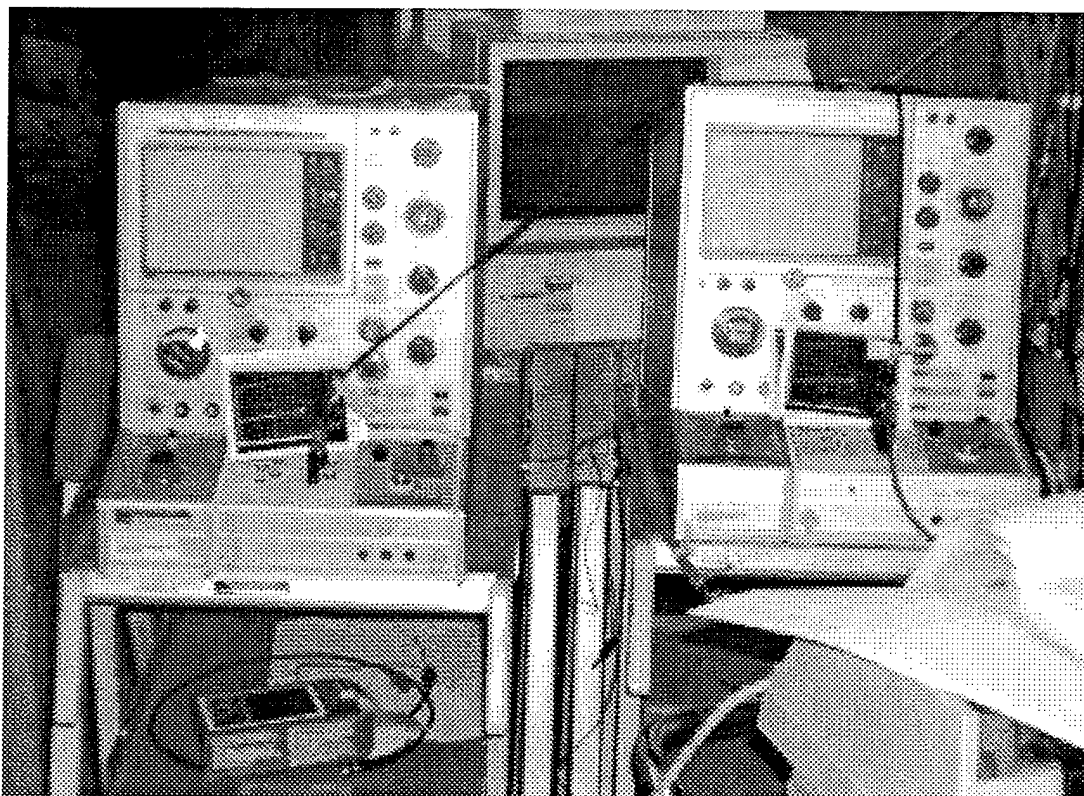


Figure 4.11. Two Tektronic 576 curve tracers utilized for measuring current gain during irradiation.

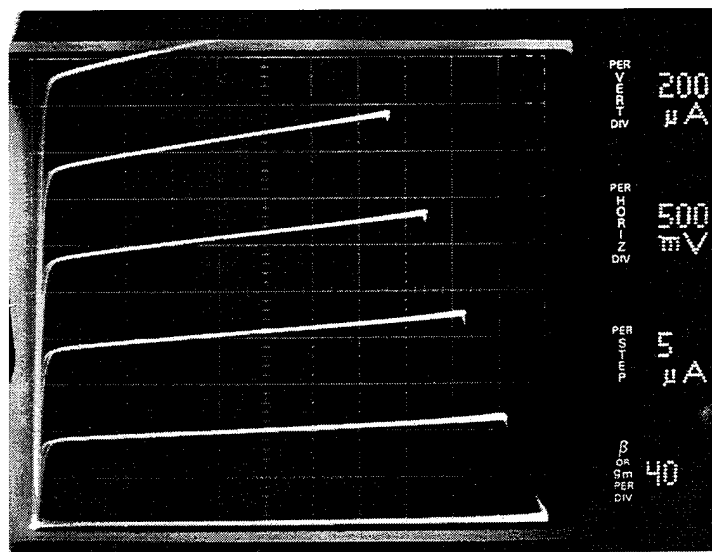
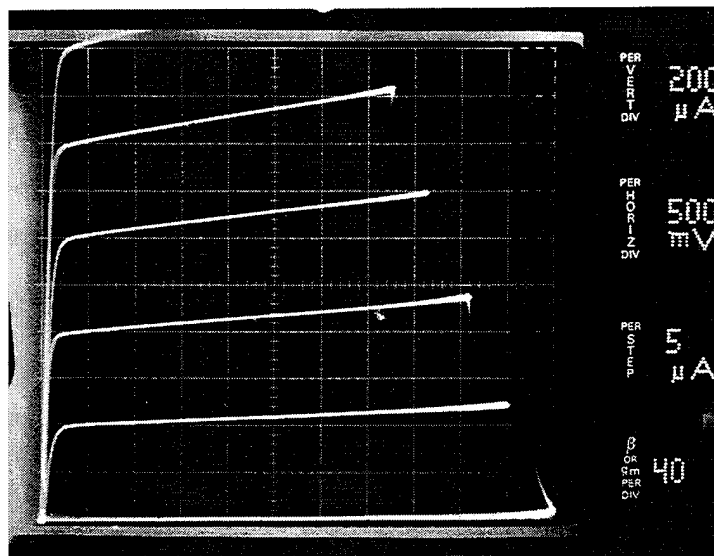


Figure 4.12. Displays of Tektronic 576 curve tracer while irradiating device-under-test.



## V. RESULTS

When analyzing the experimental results, it must be kept in mind that only the transistors in the circuit were irradiated and the other components were off chip and discrete. In the case of the opamp, the compensating capacitor and resistors received an unmeasured, but insignificant dose. This research concentrated on degradation of opamps due only to radiation damage in the transistors.

A total of five days of irradiation runs were conducted, with two days using 30 MeV electrons and three days using 60 MeV electrons. The reason for varying the electron energy was twofold. First, we wanted to see if silicon devices had any energy dependence in the 30 MeV and 60 MeV range. Secondly, at 30 MeV, it was not possible to achieve a high enough dose rate (without bringing radiation-free areas above regulations), in order to degrade the transistor  $\beta$  appreciably in the time allotted. At 60 MeV, the beam is more focused, hence less electrons leak out and contaminate the radiation-free areas.

The first run on 2 February, chip #34 was irradiated with 30 MeV electrons in the circuit configurations specified in Chapter IV (as all the runs were). The results of the dosimetry are shown in Figure (5.1). The total dose accumulated in the silicon chip was 4.7 Mrads(Si). The effect of radiation on the current gain,  $\beta$  ( $h_{FE}$ ) is shown as a function of total dose for three of the 13 transistors in Figure (5.2). Note that  $\beta$  is normalized to its initial value,  $\beta_0$ . Total dose in rad(CaF<sub>2</sub>) is taken to be equivalent to total dose rad(Si) (Refer to Chapter IV). The current gain decreased by an average of 15% for the three transistors. From previous research that modeled radiation effects on opamps, we didn't expect any measurable degradation in the

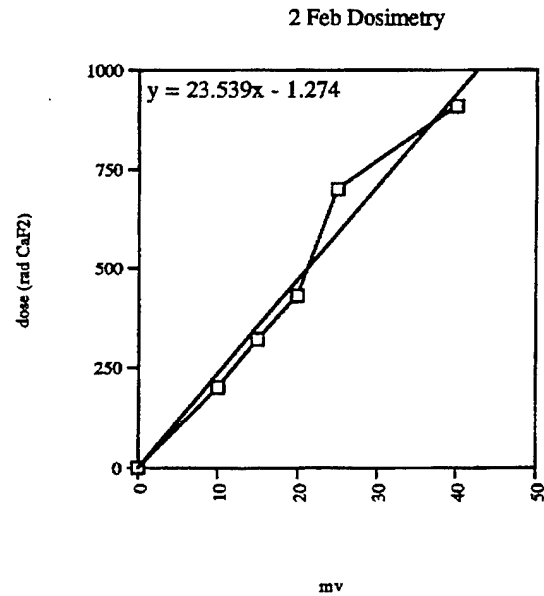


Figure 5.1. Total dose versus SEM capacitor voltage for February 2 dosimetry calibration.

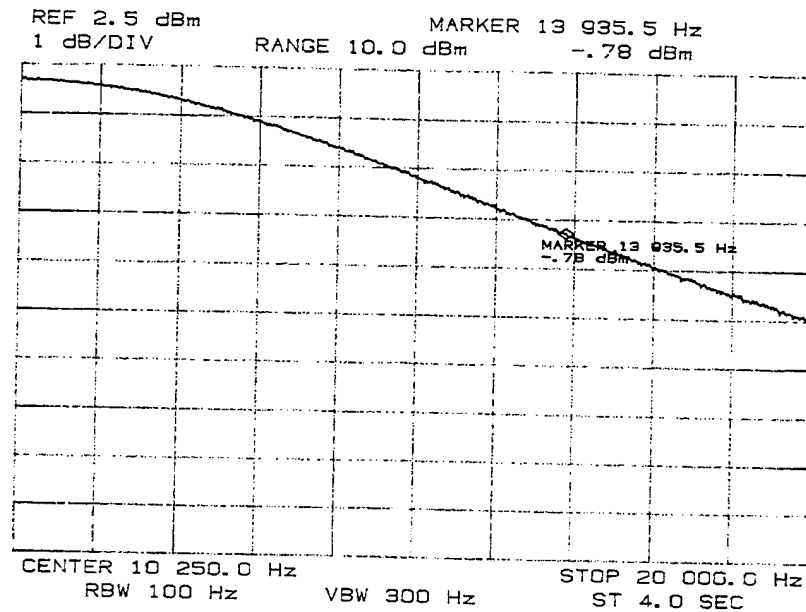


Figure 5.2. Closed loop response of opamp after transistors exposed to 4.7 Mrads(Si).



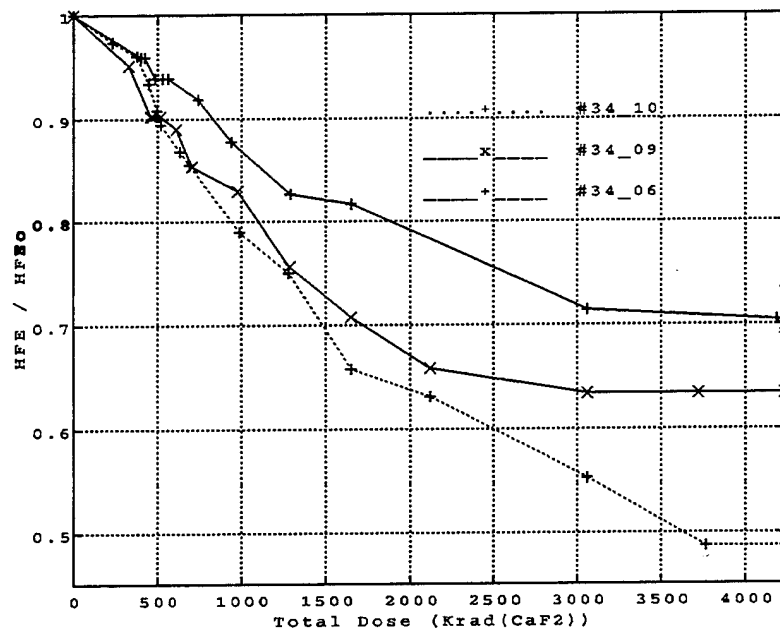


Figure 5.3. Current gain degradation as a function of total dose.  $HFE_0$  is the value at the start of the trial.

opamp parameters. Figure (5.3) shows the closed loop response for the opamp with an accumulated dose of 4 Mrad(Si). This response was monitored during the entire time of irradiation with no noticeable changes in either the 3dB frequency, Bandwidth (BW) or gain. The slew rate was checked periodically, and as expected, there was no change.

It is interesting to compare the effects of different sources of ionizing radiation. Figure (5.4) compares our experimental data from Figure (5.3) to experimental data of same type of chips irradiated with a Shepherd Co60 source. The data points label #UHF47\_83 and #UHF47\_84 were the transistors irradiated with the Co60 source up to a total dose of 1 Mrad(Si) [Ref. 38]. Of course, all we can say from this comparison is that both radiation sources have similar effects on these type of devices. Obviously, more extensive testing with controlled conditions would be required to make any kind of quantitative relationship from experimental data.

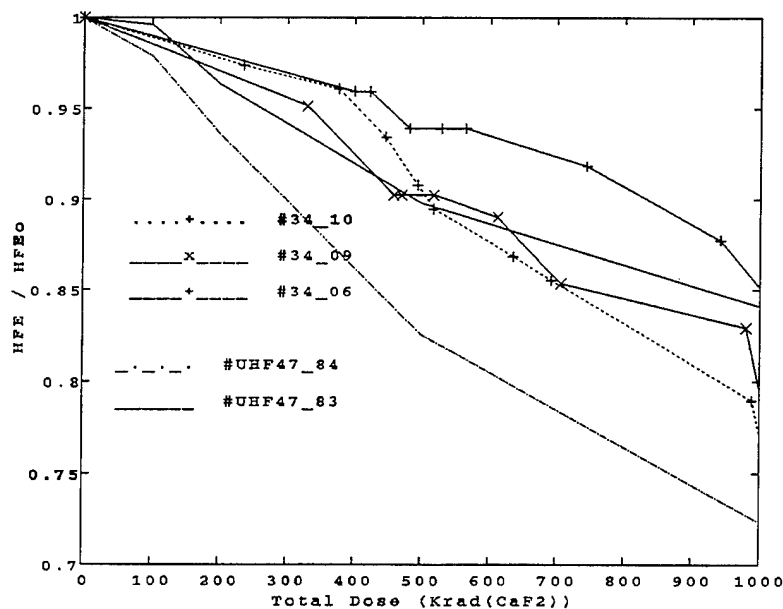


Figure 5.4. Comparison of effects of irradiation of UHF-1 transistors by a Co60 source and LINAC.

For the next radiation testing, it was decided to continue the testing again at 30 MeV with the previously irradiated chip #34, to see if we could bring the current gain down to 20% of its original value. This time the total dose achieved for the day was 17.1 Mrad(Si), a two day combined total of 21.8 Mrad(Si). The dosimetry results for the remaining trials are shown in Figure (5.5).

As in the previous trial, there was no observable change in the parameters of the opamp. Figure (5.6) represents the current degradation relative to the start of this particular run. The total dose scale represents the cumulative total dose, including that of the previous day. Figure (5.7) combines the data from the two days of radiation exposure as if it were taken in one continuous trial. At the interface of the two trials, a discontinuity can be seen in the data. It would appear if some annealing took place overnight (approximately 14 hours between trials). However, this is

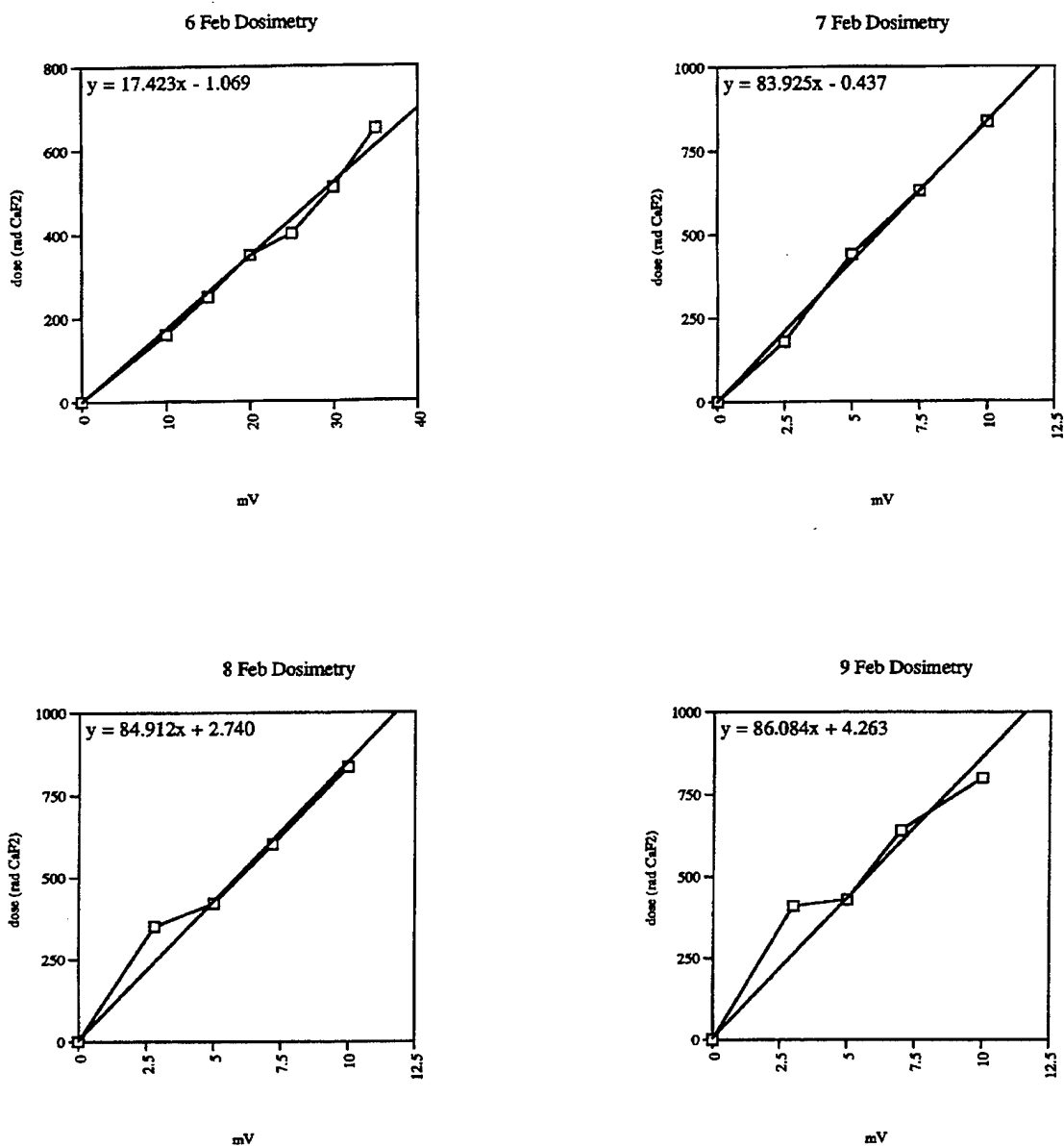


Figure 5.5. Dosimetry results for 6 through 9 February trials.

probably due more to thermal action with a little contribution to annealing. Temperature was not monitored in this experiment, but probably should be in any future testing. Previous testing with these devices suggest that little

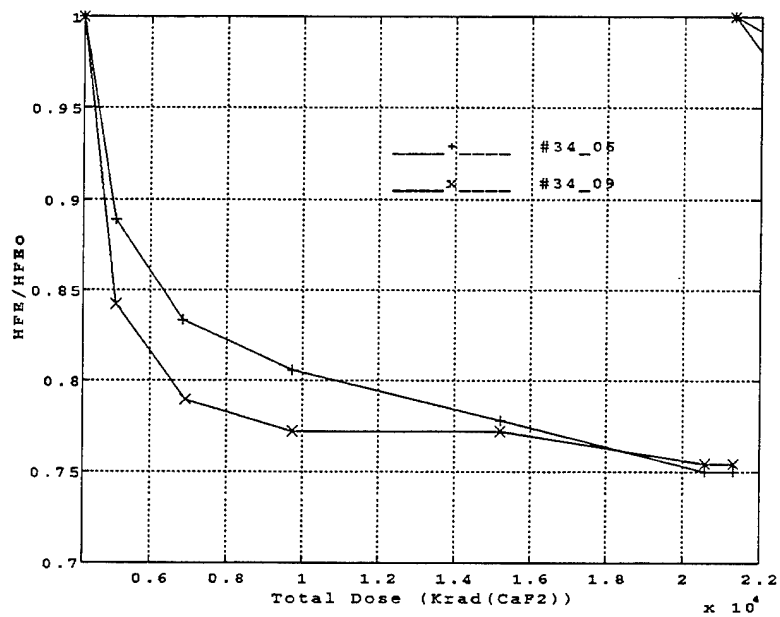


Figure 5.6. Current gain degradation as a function of total dose.  $HFE_0$  is the value at the start of the second trial.

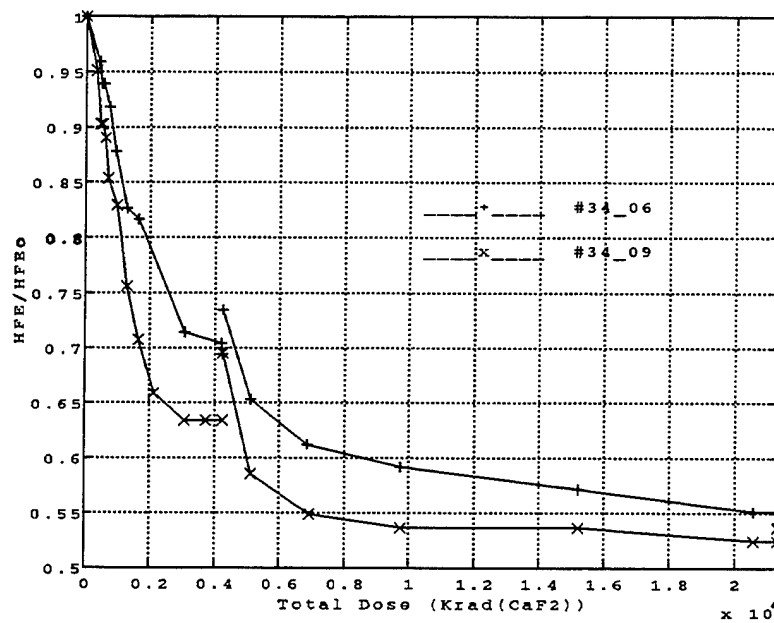


Figure 5.7. Results of two different days of irradiation with 30MeV electrons.  $HFE_0$  is the value at start of the first day.

annealing does take place. The transistors were still between 50 and 70 percent of their original gain after a two day total dose of 21.8 Mrad(Si). This still was not enough degradation to see a change in the operational amplifier characteristics. The decision was made to irradiate chip #34 a third day to degrade the current gain even more. In order to achieve a higher dose rate, ultimately a higher total dose in the time allotted, it was decided to increase the electron beam to 60 MeV. As alluded to earlier, increasing the particle fluence (to achieve a higher dose rate) at 30 MeV increased radiation levels to unacceptable values outside the laboratory.

Due to a damage to a transistor in the common emitter (CE) circuit, transistor #34\_10 was used as a replacement in the CE circuit. Therefore the remaining plots will have only two transistors plotted for  $h_{FE}$ .

The results of the 7 February trial are plotted in Figure (6.8). The three day total dose accumulation was 163 Mrad(Si). This third trial alone contributed 141.2 Mrad(Si), utilizing 60 MeV electrons. As before, Figure (5.8) reflects a current gain normalized to the starting value on the third day, while the total dose scale reflects the three day total. Figure (5.9) plots data for the trials as if it were one continuous trial. It can be seen that there was no "annealing" effect at the boundary between the second and the third trials. From this plot, it appears that the 60 MeV electrons did not change the trend of the current degradation. So far the current gain of the two transistors are still about 30% of their original value after receiving 160 Mrad(Si).

There was still no effect observed on the corresponding opamp characteristics. The gain, slewrate and 3dB frequency have not changed. Testing proceeded on new chip #30 in the same manner as before, but this time only 60 MeV electrons were to be used.

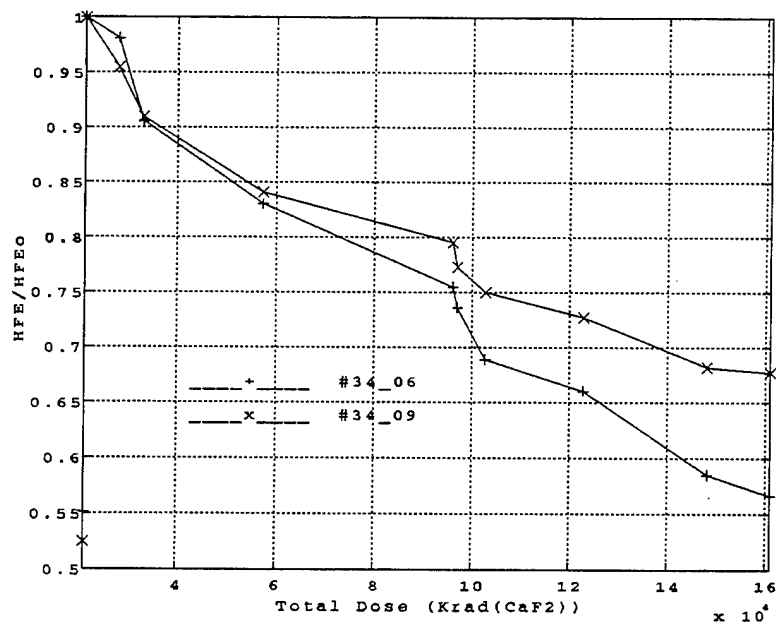


Figure 5.8. Current gain degradation as a function of total dose. HFE<sub>0</sub> is the value at the start of the trial.

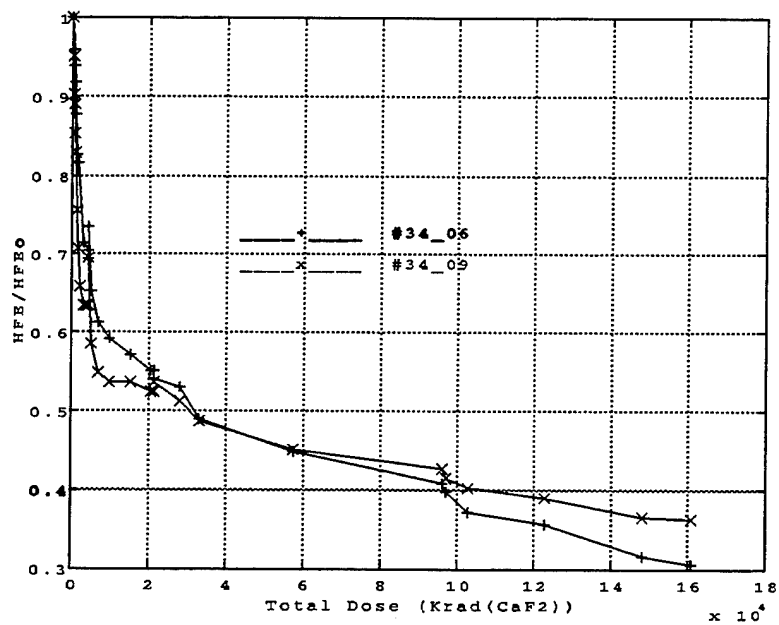


Figure 5.9. Results of three different trials utilizing chip #34.

The results of the first run on 8 February with chip #30 are plotted in Figure (5.10). The total absorbed dose at the end of this trial was 202 Mrad(Si). The current gain of the transistors was decreased to 25% and 35% of the original value for #30\_6 and #30\_9 respectively. As before, this still wasn't enough to observe any degradation in the opamp parameters. Therefore a second trial at 60 MeV was conducted on 9 February to achieve a combined two day total dose of 500 Mrads(Si). As before, these results are plotted in Figure (5.11) just for the second trial, and for the combined two trials, in Figure (5.12).

It can be seen that up until approximately 60 Mrad(Si), the two transistors degrade at almost exactly an identical rate. After about 60 Mrad(Si) total dose, the rates diverge significantly. Referring back to Figure (5.9), it can be seen that Chip #34 behaved almost the same way, at the same total dose. Chip #30\_9 has an emitter perimeter-to-area (P/A) ratio that is 6 times that of chip #30\_6, therefore one would expect that chip #30\_6 and chip #34\_6 to degrade faster than #34\_9, according to Equation (3.27). Note that chip #30\_6 and #34\_6 have the same P/A ratio as do chip #30\_9 and #34\_9.

Another observation can be made by comparing the results from two different energies of incident electron beams. Since the first run irradiated chip #34 to 4.7Mrads(Si) continuously at 30 MeV, this set of data will be plotted along with that of chip #30 which was irradiated continuously at 60 MeV to 202 Mrads(Si). The two transistors of each chip correspond to each other, therefore the P/A ratios are the same for each counterpart. This is shown in Figure (5.13).

In order to compare the effects of electron beam energy and the effects of removing the device from the radiation source for over 16 hours, Figure (5.14) is plotted. In Figure (5.14), the current gain data is plotted for both chips up to 160 Mrads(Si). It is important to note that the plot

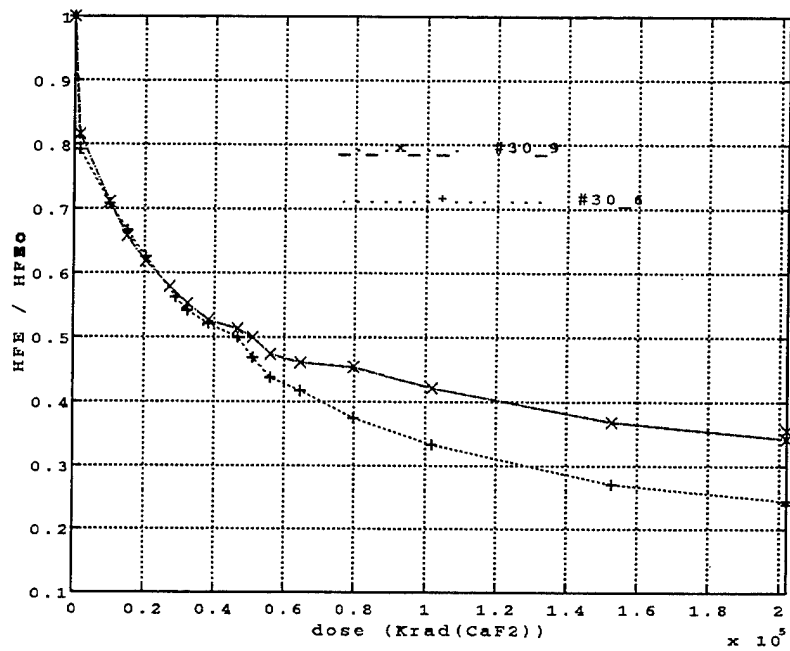


Figure 5.10. Current gain degradation as a function of total dose.  $HFE_0$  is the value of the start of the trial.

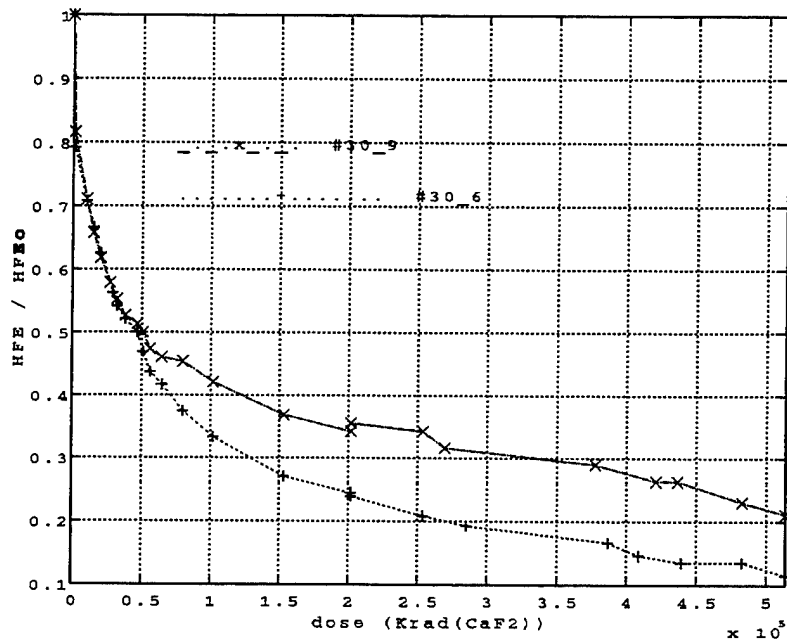


Figure 5.11. Results two different trials utilizing chip #30.



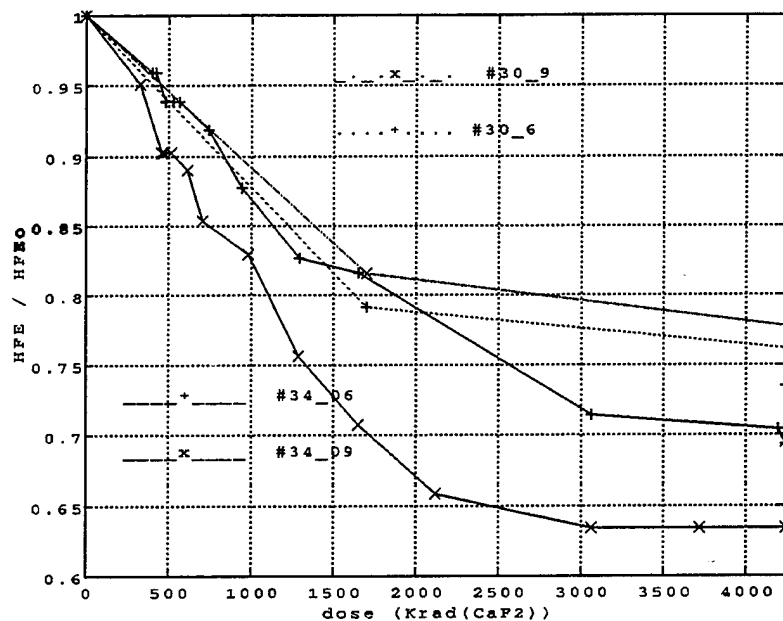


Figure 5.12. Current gain of both irradiated chips as a function of total dose up to 4.3 Mrads (Si).

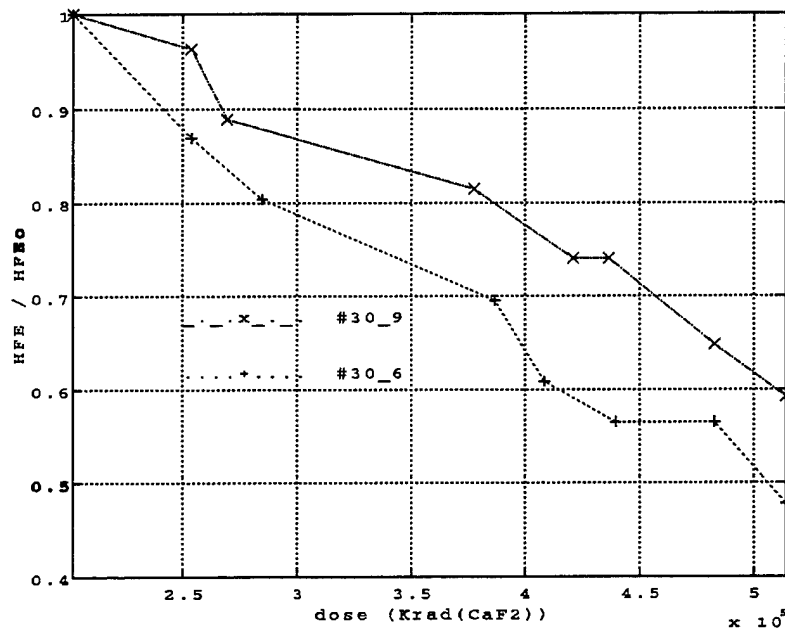


Figure 5.13. Current gain degradation as a function of total dose.  $HFE_0$  is the value at the start of the second trial.

for both transistors on chip #30 were irradiated continuously in a 60 MeV electron beam for the entire range of total dose plotted. On the other hand, the transistors on chip #34 were irradiated in three separate steps: using a 30 MeV electron beam up to 4.7 Mrads(Si), using a 30 MeV beam with the initial 4.7 Mrads(Si) and continuing to a cumulative total of 21.7 Mrads(Si), and finally using a 60 MeV beam to bring the final cumulative dose to 160 Mrads. The intervals between each step offered the device a "rest" time of 18 to 24 hours without radiation exposure.

Nothing conclusive can be drawn from this plot, however, one can see that the 3-step plot of the chip #34 transistors almost appears to be continuous. It does show a sharper rate of gain degradation than chip #30 transistors, but this could be due to the fact that they are two distinct chips which are bound to have differences even if they were made on the same wafer. This can be verified by further irradiation of the same types of devices without any "rest" times from radiation exposure.

Although not conclusive, there is strong evidence from these trials that current gain degradation vs. total dose relationship is not energy dependent in the 30 to 60 MeV range. Again, strong evidence to support this statement can be accomplished by irradiating continuously the same type of devices under a 30 MeV beam and another at 60 MeV.

Not much can be said about the opamp other than no measurable change was observed in either chip #30 or chip #34's opamp circuit. This is not completely unexpected, for it supports previous thesis research conducted on modeling radiation effects with PSpice. Figure (5.15) is the result of a simulation that degrades the current gain (or  $\beta$  in the figure) down to several levels or percentages of remaining  $\beta$ . A simulation is run for a generic  $\mu$ A741 opamp utilizing these degraded transistor models. It can be seen that to obtain

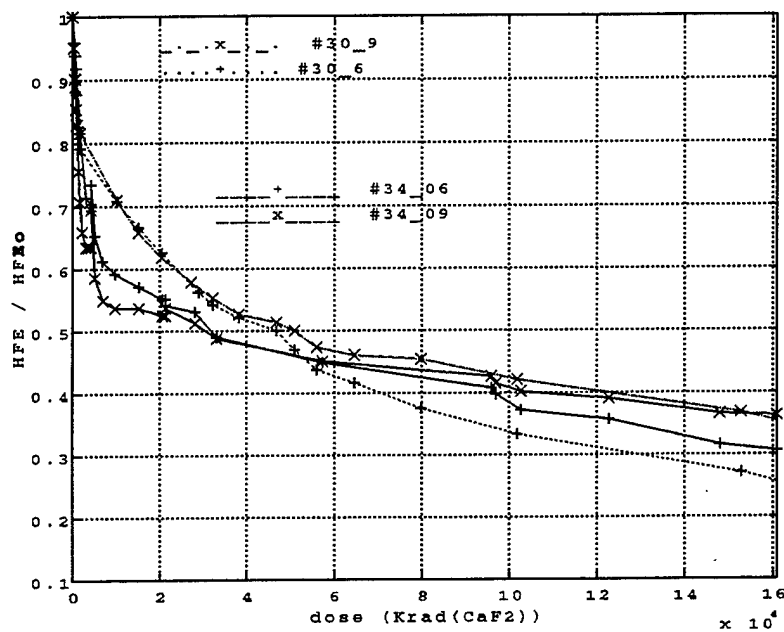


Figure 5.14. Cumulative current gain data for both chips up to 160 Mrad(Si).

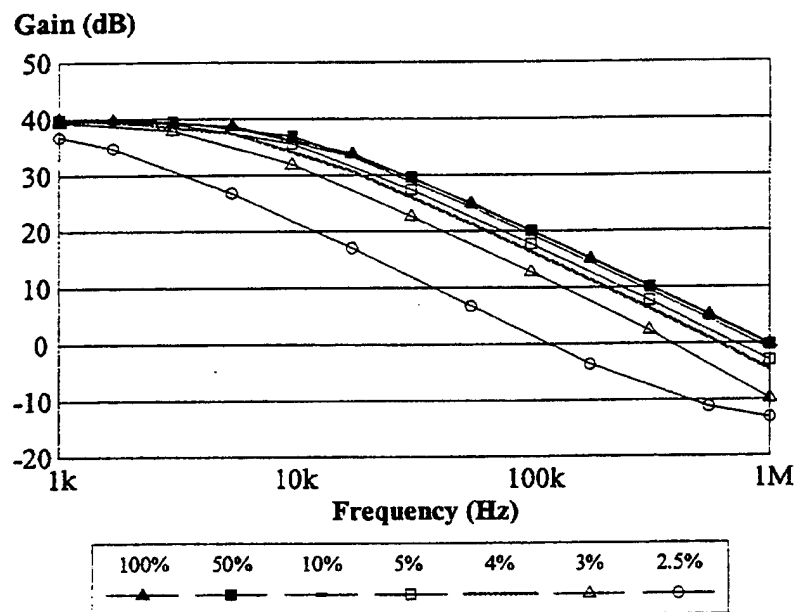


Figure 5.15.  $\mu$ A741 operational amplifier degradation curves as function of percent remaining current gain. From Ref. [39, p. 65].

observable degradation in the opamp gain, the transistor current gains must degrade to 5% of their original value. In this research, we were only able to bring the current gains down to an average of 30% of the original value, therefore we did not see any degradation in opamp parameters.

It should be noted that we did not include data from the common emitter circuit, specifically the ac voltage measurements corresponding to the base and collector currents. This is because the data was not consistent. There were severe fluctuations when the klystrons were turned on and the initial calculations gave a value of  $f_T$  that was many orders of magnitude lower than from the manufacturer's specification. There was indication that  $f_T$  did decrease with total dose as expected, but no useful data was obtainable.

## VI. CONCLUSIONS AND RECOMMENDATIONS

This research was intended to help create a more accurate model of bipolar transistors using data derived from experiment. Because of limited time and limited number of devices, the quantitative data obtained from this research is not useful for forming an accurate model. Many repeated runs under varying conditions and configurations would be required to form an accurate quantitative description. However, the procedures investigated can be used in establishing a baseline for further improved experiments.

Some interesting conclusions can be drawn from this investigation. First, there is strong evidence that the current degradation in the UHF-1 Harris bipolar transistor is not dependent on the energy of the incident electron beam, at least between the energies of 30 MeV and 60 MeV. Previous research at NPS and the Jet Propulsion Laboratory has shown this to be true for other semiconductor devices in the energy ranges of 16-84 MeV [Ref. 40, p. 4] [Ref. 41, p. 11] [Ref. 42, p. 19]. Note that shielding effects are not included here.

Secondly, this investigation showed that in-situ measurements for transistors and opamps are possible, utilizing a single die, thus ensuring a uniform radiation distribution. The resulting displays on the spectrum analyzer and curve tracers showed almost non-observable levels of noise, even with the LINAC kylstrons turned on.

It was surprising that the transistors retained as much as 25-30% of their original gain after being exposed to over 500 Mrads (Si). Similar work done using the NPS LINAC, found that integrated opamps of different technology survived after receiving doses of over 68 Mrads(Si) [Ref. 42, p. 92]. Survival under these high doses is questionable and should be further investigated with the same type of devices used in this research. Of interest is the data in Figure (5.4), where

the total dose response using a  $\text{CO}_{60}$  source compared favorably with that of the NPS LINAC. However, nothing is known of the effects of 500 Mrad(Si) using a  $\text{CO}_{60}$  source.

Continuation of this research should include investigation into a noise resistant method to measure the transition frequency  $f_T$ . This is necessary in order to understand the effect of radiation on the parasitic capacitances inherent in the transistor. In addition, further irradiation trials should include testing these SOI bipolar devices to the same doses used in this experiment, but without any "rest time" to see if this has an effect on the overall total dose response.

In order to understand the effects of capacitances and resistors used in integrated circuits, these devices should be irradiated in a similar fashion as was done here. The ideal test device required to accomplish the goal of obtaining an effective model for an opamp would be a die with a standard opamp built on it along with individual transistors having the same dimensions and design as those used in the opamp. This will ensure that all components of the opamp and the individual transistors will be exposed to the same radiation and the responses to both can be compared.

## APPENDIX. GLOSSARY OF SYMBOLS AND TERMS

Due to differences in symbology and terms used in various sources, this appendix provides a compact list of symbols and terms along with their definitions as used in this paper.

$E$	- energy
$e$	- charge of one electron equivalent to $1.6 \times 10^{-19}$ Columbs
$m$	- mass
$h$	- Plank's constant, $4.136 \times 10^{-15}$ eV·sec
$\nu$	- frequency
$v$	- velocity
$V_0$	- stopping potential
$p$	- momentum
$\lambda$	- wavelength, or magnetic (invariant) latitude, in the case of McIlain's L parameter
$c$	- speed of light, $2.9979 \times 10^8$ meters/sec
$k$	- Boltzmann constant, $8.617 \times 10^{-5}$ eV/°K
$T$	- temperature (300K° usually considered room temperature)
$\epsilon_0$	- permittivity of free space, $8.854 \times 10^{-12}$ C <sup>2</sup> ·N <sup>-1</sup> ·m <sup>-2</sup>
$Z$	- atomic number
$n$	- neutron
$p$	- proton
$L$	- McIlain's L parameter, approximately the giocentric distance of a field line in the geomagnetic equator
$R$	- radius of the earth
$M$	- geomagnetic dipole moment
$B$	- magnetic field
$E_f$	- Fermi energy
$N_e$	- density of states per unit volume

$m_e^*$	- effective mass of an electron in a given state
$m_p^*$	- effective mass of a hole in in a given state
$n_o$	- number density of states for electrons (carriers/cm <sub>3</sub> )
$p_o$	- number density of states for holes (carriers/cm <sup>3</sup> )
$n_i$	- intrinsic carrier density
$N_D$	- donor concentration
$N_A$	- acceptor concentration
$\tau$	- mean free path between collisons
$\mu$	- carrier mobility
$\bar{J}$	- current density, Amperes/m <sup>2</sup>
$\bar{j}$	- particle current
$D_{n,p}$	- electron, hole diffusion coefficient
$g_o$	- carrrier thermal equilibrium generation rate
$C_{n,p}$	- electron, hole capture cross-sections
$N_t$	- density of recombination centers (traps)
$l$	- width of depletion layer
$L$	- diffusion length
$C_j$	- junction capacitance
$C_d$	- diffusion capacitance
$C_\mu$	- collector-base capacitance
$C_\pi$	- emitter-base capacitance
$\sigma$	- coductivity
$\delta_{p,n}$	- excess carrier concentrations
$\beta$	- BJT current gain
$S_p$	- recombination velocity
$W$	- base width
$f_T$	- transition frequency
$Q$	- total electric charge



$D$  - total or absorbed dose  
 $\psi$  - energy fluence  
 $S_{col}$  - mass collision stopping power  
 $\mu_{en}/\rho$  - mass energy absorption coefficient



## LIST OF REFERENCES

1. Rasmussen, R. D., "Spacecraft Electronics Design for Radiation Tolerance," *Proc. IEEE*, vol. 76, pp. 1423-1442, Nov. 1988.
2. Pease, R. L., "Radiation Testing of Semiconductor Devices for Space Electronics," *Proc. IEEE*, vol. 76, pp. 1510-1526, Nov. 1988.
3. Tipler, P. A., *Modern Physics*, Worth Publishers Inc., New York, NY, 1978.
4. Mckelvey, J. P., *Solid State and Semiconductor Physics*, Harper & Row, New York, NY, 1966.
5. Sears, F. W., *University Physics*, Addison-Wesley Publishing Co., Menlo Park, CA, 1982.
6. Segre, E., *Nuclei and Particles*, W. A. Benjamin Inc., New York, NY, 1964.
7. Ricketts, L. W., *Fundamentals of Nuclear Hardening of Electronic Equipment*, John Wiley & Sons, Inc., New York, NY, 1972.
8. Srour, J. R., "Radiation Effects on Microelectronics in Space," *Proc. IEEE*, vol. 76, pp. 1443-1469, Nov. 1988.
9. Hess, W. N., *The Radiation Belt and Magnetosphere*, Blaisdell Publishing Co., Waltham, MA, 1968.
10. Corliss, W. R., *Space Radiation*, United States Atomic Energy Commission Office of Information Services, 1968.
11. Friedlander, M. W., *Cosmic Rays*, Harvard University Press, Cambridge, MA, 1989.
12. Reitz, J. R., *Foundations of Electromagnetic Theory*, Addison-Wesley Publishing Co., Reading, MA, 1979.
13. O. Heinz, R. C. Olsen, *Introduction to the Space Environment*, Naval Postgraduate School Course Notes for PH 2514, Monterey, CA, 1993.
14. Stassinopoulos, E. G., "The Space Radiation Environment for Electronics," *Proc. IEEE*, vol. 76, 1423-1442, Nov. 1988.
15. Tabbert, C., "A Historical Perspective," *Space Product News*, Harris Semiconductor, Melbourne, FL, Sept. 1993.

16. N.A. Nelson, Lenehan, J.M., "Space Systems Overview," 1993 *IEEE Aerospace Applications Conference Digest*, pp. 1-150 Apr. 1993.
17. Kittel, C., *Introduction to Solid State Physics*, John Wiley & Sons Inc., New York, NY, 1986.
18. Pulfrey, D. L., *Introduction to Microelectronic Devices*, Prentice Hall, Inc., Englewood Cliffs, NJ, 1989.
19. Rudie, N. J., *Principles and Techniques of Radiation Hardening*, Vol. 3 & 4, Western Periodicals Co., North Hollywood, CA, 1986.
20. Larin, F. *Radiation Effects in Semiconductor Devices*, John Wiley & Sons, New York, NY, 1968.
21. Messenger, G. C., *The Effects of Radiation on Electronic Systems*, Von Nostrand Reinhold Company, Inc., New York, NY, 1986.
22. Antognetti, P., *Semiconductor Device Modeling with Spice*, McGraw-Hill Inc., New York, NY, 1988.
23. Till, W. C., *Integrated Circuits: Materials, Devices, and Fabrication*, Prentice-Hall, Englewood Cliffs, NJ, 1982.
24. Dalven, R., *Introduction to Solid State Physics*, Plenum Press, New York, NY, 1990.
25. A. S. Sedra, K. C. Smith, *Microelectronic Circuits*, Saunders College Publishing, Chicago, IL, 1991.
26. R. N. Nowlin, E. W. Enlow, R. D. Schrimpf, W. E. Combs, "Trends in the Total-Dose Response of Modern Bipolar Transistors," *IEEE Trans. Nucl. Sci.*, vol. NS-39, pp. 2026-2035, Dec. 1992.
27. Flament, O., "Radiation Effects on SOI Analog Device Parameters," *IEEE Trans. Nucl. Sci.*, vol. NS-41, pp. 565-571, June 1994.
28. O'Reilly, P. J., *Effects of 30 MeV Electron Irradiation on InGaAsP LEDs and InGaAs Photodiodes*, Master's Thesis, Naval Postgraduate School, Monterey, CA, June 1986.
29. M. T. Barnett, W. J. Cunneen, *Design and Performance of the Electron Linear Accelerator at the U. S. Naval Postgraduate School*, Master's Thesis, Naval Postgraduate School, Monterey, CA, June 1966.

30. Lane, T. F., *A Study of Effects of High Energy Electron Radiation on Selected Electronic Devices*, Master's Thesis, Naval Postgraduate School, Monterey, CA, June 1972.
31. Foley, J. K., *30 MeV Electron Beam Irradiation Effects on GaAsP LEDs*, Master's Thesis, Naval Postgraduate School, Monterey, California, June 1985.
32. Kerris, K. G., "Practical Dosimetry for Radiation Hardness Testing," *IEEE Nuclear and Space Radiation Effects Conference Short Course*, New Orleans, LA, July 1992.
33. Beutler, L. J., "Dosimetry in LINAC Electron-Beam Environments," *IEEE Trans. Nucl. Sci.*, vol. NS-38, pp. 1171-1179, Dec. 1991.
34. Victoreen Inc., *Instruction Manual for Model 2800 Thermoluminescence Dosimeter Reader*, Part No. 2800-1-1B, Rev. 9/86.
35. Kerris, K. G., "The Energy Dependence of  $\text{CaF}_2\text{:Mn}$ /Teflon Thermoluminescent Dosimeters," *IEEE Trans. Nucl. Sci.*, vol. NS-37, pp. 1752-1755, Dec. 1990.
36. Davis, C., "UHF-1: A High Speed Complementary Bipolar Analog Process on SOI," *IEEE 1992 Bipolar Circuits and Technology Meeting*, Piscataway, NJ, 1992.
37. Goodenough, F., "Linear ICs Attain 8-GHz NPNs, 4-GHz PNP's," *Electronic Design*, Dec. 1991.
38. Naval Surface Warfare Center, Crane Division, Report #NSWC-93- 6054-0022, Crane, IN, Aug. 1993.
39. Baczuk, R. L., "PSpice Simulatio of Total Dose Effects on Composite and Single Operational Amplifiers," Master's Thesis, Naval Postgraduate School, Monterey, CA, Sept. 1994.
40. Dyer, J. N., "Some Effects of Electron Irradiation on Integrated Circuits," NPS-61DY71121B, Naval Postgraduate School, Monterey, CA, Dec. 1971.
41. Dyer, J. N., "Some Effects of Electron Irradiation on MOS Field Effect Transistors," NPS-61DY72081B, Naval Postgraduate School, Monterey, CA, Sept. 1972.

42. Sage, S.E., "Total Dose Radiation Effects on Bipolar Composite and Single Operational Amplifiers Using a 30 MeV Linear Accelerator," Master's Thesis, Naval Postgraduate School, Monterey, CA, 1988.

# INITIAL DISTRIBUTION LIST

	No. Copies
1. Defense Technical Information Center Cameron Station Alexandria, VA 22304-6145	2
2. Library, Code 52 Naval Postgraduate School Monterey, CA 93943-5101	2
3. Chairman, Code EC Department of Electrical and Computer Engineering Naval Postgraduate School Monterey, CA 93943-5121	1
4. Professor S. Michael, Code EC/Mi Department of Electrical and Computer Engineering Naval Postgraduate School Monterey, CA 93943-5121	4
5. Professor D. Fouts, Code EC/Fs Department of Electrical and Computer Engineering Naval Postgraduate School Monterey, CA 93943-5121	1
6. Commander (6054 Bill Combs) NAVSURFWARCENDIV 300 Highway 361 Crane, IN 47522-5001	1
7. LT Donald R. Brittain, Jr. P.O. Box 262 Lakeville, PA 18438	1